

Impacting Pancreatic Cancer Therapy in Heterotypic *in Vitro* Organoids and *in Vivo* Tumors with Specificity-Tuned, NIR-Activable Photoimmunonanoconjugates: Towards Conquering Desmoplasia?

Girgis Obaid,[†] Shazia Bano,[†] Srivalleesha Mallidi,^{†,‡} Mans Broekgaarden,[†] Jerrin Kuriakose,[†] Zachary Silber,[†] Anne-Laure Bulin,[†] Yucheng Wang,[†] Zhiming Mai,[†] Wendong Jin,[†] Diane Simeone,[‡] and Tayyaba Hasan^{*,†,§}

[†]Wellman Center for Photomedicine, Massachusetts General Hospital and Harvard Medical School, Boston, Massachusetts 02114, United States

[‡]Department of Surgery and Department of Pathology, Perlmutter Cancer Center, New York University Langone Health, New York, New York 10016, United States

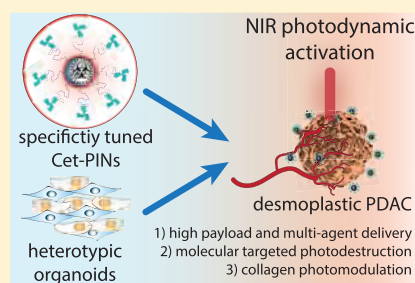
[§]Division of Health Sciences and Technology, Harvard University and Massachusetts Institute of Technology, Cambridge, Massachusetts 02139, United States

Supporting Information

ABSTRACT: Despite untiring efforts to develop therapies for pancreatic ductal adenocarcinoma (PDAC), survival statistics remain dismal, necessitating distinct approaches. Photodynamic priming (PDP), which improves drug delivery and combination regimens, as well as tumor photodestruction are key attributes of photodynamic therapy (PDT), making it a distinctive clinical option for PDAC. Localized, high-payload nanomedicine-assisted delivery of photosensitizers (PSs), with molecular specificity and controlled photoactivation, thus becomes critical in order to reduce collateral toxicity during more expansive photodynamic activation procedures with curative intent. As such, targeted photoactivable lipid-based nanomedicines are an ideal candidate but have failed to provide greater than two-fold cancer cell selectivity, if at all, due to their extensive multivariant physical,

optical, and chemical complexity. Here, we report (1) a systematic multivariant tuning approach to engineer (Cet, anti-EGFR mAb) photoimmunonanoconjugates (PINs), and (2) stroma-rich heterotypic PDAC *in vitro* and *in vivo* models incorporating patient-derived pancreatic cancer-associated fibroblasts (PCAFs) that recapitulate the desmoplasia observed in the clinic. These offer a comprehensive, disease-specific framework for the development of Cet-PINs. Specificity-tuning of the PINs, in terms of PS lipid anchoring, electrostatic modulation, Cet orientation, and Cet surface densities, achieved ~16-fold binding specificities and rapid penetration of the heterotypic organoids within 1 h, thereby providing a ~16-fold enhancement in molecular targeted NIR photodestruction. As a demonstration of their inherent amenability for multifunctionality, encapsulation of high payloads of gemcitabine hydrochloride, 5-fluorouracil, and oxaliplatin within the Cet-PINs further improved their antitumor efficacy in the heterotypic organoids. In heterotypic desmoplastic tumors, the Cet-PINs efficiently penetrated up to 470 μm away from blood vessels, and photodynamic activation resulted in substantial tumor necrosis, which was not elicited in T47D tumors (low EGFR) or when using untargeted constructs in both tumor types. Photodynamic activation of the Cet-PINs in the heterotypic desmoplastic tumors resulted in collagen photomodulation, with a 1.5-fold reduction in collagen density, suggesting that PDP may also hold potential for conquering desmoplasia. The *in vivo* safety profile of photodynamic activation of the Cet-PINs was also substantially improved, as compared to the untargeted constructs. While treatment using the Cet-PINs did not cause any detriment to the mice's health or to healthy proximal tissue, photodynamic activation of untargeted constructs induced severe acute cachexia and weight loss in all treated mice, with substantial peripheral skin necrosis, muscle necrosis, and bowel perforation. This study is the first report demonstrating the true value of molecular targeting for NIR-activable PINs. These constructs integrate high payload delivery, efficient photodestruction, molecular precision, and collagen photomodulation in desmoplastic PDAC tumors in a single treatment using a single construct. Such combined PIN platforms and heterocellular models open up an array of further multiplexed combination therapies to synergistically control desmoplastic tumor progression and extend PDAC patient survival.

KEYWORDS: Nanoengineering, photoimmunonanoconjugates, pancreatic ductal adenocarcinoma, NIR photodynamic activation



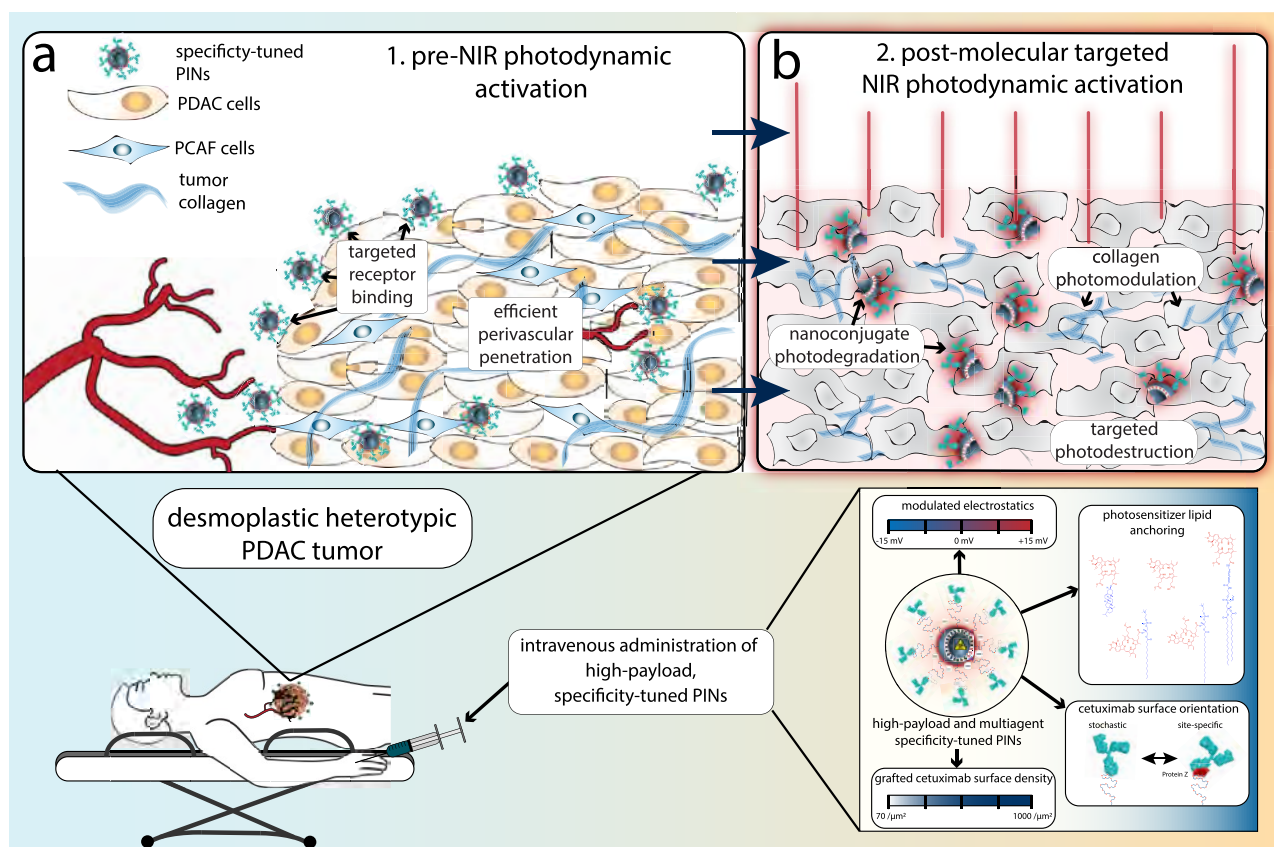
Pancreatic ductal adenocarcinoma (PDAC) is a particularly stubborn malignancy with dismal prognoses. Five-year patient survival rates are less than 5%, and even with the most

Received: February 27, 2019

Revised: September 11, 2019

Published: September 13, 2019

Scheme 1. Molecular Targeted NIR Photodynamic Activation in Heterotypic Desmoplastic PDAC using Specificity-Tuned Photoimmunonanoconjugates^{a,b}



^a(a) Conceptual representation of EGFR-specific, molecular targeted NIR photodynamic activation in heterotypic desmoplastic PDAC that results in nanoconjugate disintegration, targeted necrosis of desmoplastic tumor tissue, and photomodulation of collagen; (b) Effective targeted photodestruction of desmoplastic PDAC tissue is achieved by high-payload, cetuximab directed photoimmunonanoconjugates (PINs), which have been tuned to achieve the highest degree of molecular specificity. ^bThree-dimensional (3D) representations of Cetuximab (IgG2a, Protein Data Bank (PDB) ID: 11GT)²⁵ and Protein Z (Z domain, Protein A from *Staph. Aureus*, PDB ID: 2SPZ)²⁶ were projected using Jmol: an open-source Java viewer for chemical structures in 3D.²⁷

aggressive and toxic treatment regimens, such as FOLFIRINOX, median survival does not exceed 11.1 months.^{1,2} PDAC is characterized by desmoplasia, a reaction leading to dense stromal deposition of collagen-rich extracellular matrix, predominantly by activated pancreatic cancer-associated fibroblasts (PCAFs).^{3–5} Desmoplasia limits the delivery of therapeutic agents, including nanomedicines, contributing to treatment resistance.⁶ Ideally, the preclinical models used to evaluate novel therapeutics for PDAC must capture and present features of desmoplasia. We demonstrate in this study that this is made feasible by heterotypic PDAC models that incorporate patient-derived PCAFs.

Photodynamic activation of photosensitizers (PSs) is capable of inducing significant and light dose-dependent tumor necrosis in PDAC patients using current clinical regimens for photodynamic therapy (PDT).⁷ In addition, a cooperative mechanistic photodynamic priming (PDP) of the tumor microenvironment improves the outcomes of subsequent combination therapies.^{7–11} The priming role of PDT has not been studied in depth, although it holds considerable promise for microenvironmental modulation such as increased drug permeability.^{11–13} This becomes critical as nanomedicines evolve, with prior evidence that PDP improves the delivery of Doxil and liposomal irinotecan to tumors.^{11,12} The ideal

photoactivable nanomedicine would therefore combine features of PDAC tumor destruction with photodynamic priming using a single construct and a single near-infrared (NIR) photodynamic activation procedure.

PDT regimens in current early phase clinical trials achieve controllable zones of tumor necrosis but exhibit some adverse toxicities including prolonged skin phototoxicity, nausea, photosensitivity, skin hyperpigmentation, and higher healthy tissue accumulation of the PS that increases the risk of off-target photodamage.¹⁴ However, as clinical procedures evolve towards curative PDT regimens, higher PS doses and expansive regions of irradiation are required. Administration of higher PS doses has resulted in cases of hepatotoxicity resulting from hemolysis, dysregulated blood pressure and heart rate, and cardiorespiratory events leading to fatalities.^{15,16} Furthermore, expansive illumination protocols around critical anatomical sites have led to collateral phototoxicity. For example, PDT of PDAC tumors involving the gastroduodenal artery resulted in cases of gastrointestinal bleeds.¹⁴ If expansive and complete PDAC treatment is to be achieved safely, higher PS payload delivery to tumors is critically needed in addition to molecular precision of photodamage. Molecular targeted photodynamic activation can enhance the tolerability to higher light doses during PDT,¹⁷

thereby maximizing the extent of PDAC tumor damage while sparing critical healthy vicinal tissue.

Nanomedicines are an attractive and clinically proven strategy to reduce the systemic toxicity of chemotherapeutics while increasing localized tumor delivery.¹⁸ Photonanomedicines, light-activable nanotherapeutics, combine the attractive tumor-delivery and anticancer agent tolerability properties of nanomedicines with the potent antitumor potential of PDT.^{7,19} Considering the toxicities associated with high PS administration, localized high-payload delivery within desmoplastic PDAC tumors using photonanomedicines thus becomes critical, as well as spatiotemporally controlled photoactivation, to reduce collateral toxicity. Ideally, the highest-payload nanoparticle PS carrier would be constituted of the photodynamic agent itself. This simplified nanoparticle approach is also advantageous in that it circumvents issues related to complex nanosystems and thus simplicity has been correlated with impact.²⁰ An elegant example of such high-payload photonanomedicines includes metal-organic frameworks, which are ordered in a conformation that preserves the photochemistry of the photosensitizer.²¹ However, introducing functionality to photonanomedicines naturally increases the complexity of the nanosystem, and a balance between rigorous and reproducible fabrication, functionality, and simplicity becomes critical.²² Furthermore, the clinical relevance of multifunctional photonanomedicines is of paramount importance for expediting the translation of critically needed PDAC treatments. Visudyne is the first clinically approved lipid-based photonanomedicine formulation of benzoporphyrin derivative (BPD) that has already shown superior performance in PDAC patients.⁷ Given that 80% of pancreatic cancers are unresectable,²³ Visudyne-PDT has been shown to be particularly powerful in PDAC clinical trials, with one instance of converting an unresectable PDAC tumor into one that underwent R0 Whipple's pancreaticoduodenectomy.⁷

The ultimate goal and challenge is to thus strike a balance between efficacy and toxicity. This study is a significant stride toward that goal by presenting photoimmunonanoconjugates (PINs) that can efficiently destroy desmoplastic PDAC tumors with the molecular precision of antibody therapeutics while also modulating the tumor stroma by reducing collagen density (Scheme 1). A number of agents that modulate the stroma in PDAC are currently being tested in clinical trials, such as the angiotensin inhibitor losartan, the micropinocytosis inhibitor hydroxychloroquine, enzymes that digest hyaluronic acid and agonists of the retinoic acid receptor and the vitamin D receptor.^{5,24} In this paper, we present a single therapeutic NIR-activable nanoconjugate with collagen-modulating characteristics, high-payload drug delivery, and molecular targeted tumor killing potential that promises to enhance the safety of curative clinical PDT procedures.

Particularly in the case of problematic diseases such as desmoplastic PDAC, the high-throughput *in vitro* testing routines used to guide the development of these specificity-tuned PINs must be able to recapitulate the physical and biochemical barriers presented by clinical manifestations of the disease. Not only must there be intelligence in the design of such complex nanomedicines but there must also be creativity in the design of disease-recapitulating, high-throughput testing platforms to provide a meaningful framework for comprehensive evaluation. In this study, we develop heterotypic PDAC organoids and *in vivo* tumors using MIA PaCa-2 cancer cells and patient-derived PCAFs as an intelligent, disease-specific model to guide the

engineering and evaluation of molecular targeted, NIR activable PINs.

Such complex molecular targeted, NIR-activable PINs require diligence in their fabrication and strategic modulation of their codependent constituents to simultaneously capture and retain the following salient features of optimal PINs: molecular specificity, high-payload delivery, and potent photochemical activity. Although previous attempts to provide molecular specificity for lipidic nanoconstructs carrying PSs have shown up to two-fold improvements in binding specificities and phototoxicity in cell cultures, many have failed, and little evidence of *in vivo* efficacy in solid tumors has been demonstrated to date.^{28–36} This is a direct result of the complexity of preparing functionalized nanoconjugates that incorporate light-activable features. To encompass the intricacies of fabricating molecular targeted PINs that retain the motivating features described above, we adopt a rational multivariant engineering approach to engineer specificity-tuned, Cetuximab (Cet; anti-EGFR mAb) targeted nanolipid formulations of BPD. These PINs are inspired by the promising high-payload clinical formulation of BPD, Visudyne, and the molecular targeted clinical antibody Cet. With EGFR expression observed in up to 85% of patients with PDAC,³⁷ and anti-EGFR antibodies currently being used for image-guided surgical resection of PDAC in the clinic,³⁸ Cet becomes an ideal and opportune candidate for molecular targeted NIR photodynamic activation.

The interdependent factors of the optimal Cet-PIN that we show to be critical, and have modulated for maximal specificity, include the lipidation and stable membrane-anchoring of BPD, tuning the surface electrostatics to minimize heterogeneity in cellular uptake, and controlling Cet surface orientations and densities using either site-specific Protein Z-mediated, or stochastic copper-free click chemistry. We show in this study that the specificity-tuned Cet-PINs that are capable of destroying desmoplastic heterotypic PDAC organoids and xenografted tumors *in vivo* combine a lysophospholipid-anchored variant of BPD, an anionic ζ -potential of -20.7 ± 1.6 mV, and a surface density of 517.5 ± 138.6 Cet per μm^2 of stochastically oriented Cet. As compared to direct BPD-Cet photoimmunonanoconjugates (PICs) with a maximum payload of 10 BPD molecules per Cet,³⁹ the specificity-tuned Cet-PINs engineered in this study retained a striking 60% of the hydrophobic PS's photodynamic activity and remained tumor-specific and colloidally stable at a high payload of ~ 600 BPD molecules per construct. Although recent elegant efforts to maximize the PS payloads of PICs have achieved up to 15 PS molecules per antibody,⁴⁰ the Cet-PINs offer higher PS payloads and offer the potential of multiagent delivery. Our specificity-tuned Cet-PINs demonstrated the highest ever reported cancer cell binding specificities of all targeted photoactivable nanoconstructs, with up to 100-fold preferential binding, and up to 30-fold improvements in EGFR-specific photokilling of MIA PaCa-2 cells in monolayer. More importantly, the specificity-tuned Cet-PIN demonstrated up to 16.9-fold binding specificities in the heterotypic PDAC organoids containing PCAFs and rapidly permeated the organoids within 1 h of incubation. This translated to a remarkable ~ 16 -fold enhancement in molecular targeted photodynamic destruction that was agnostic to PCAF-induced treatment resistance in the heterotypic organoids.

Using non-invasive *in vivo* photoacoustic imaging, we further show that the perivascular tumor penetration of the optimized Cet-PINs ranged from 174–473 μm within heterotypic

multivariant specificity-tuning of Cet-PINs

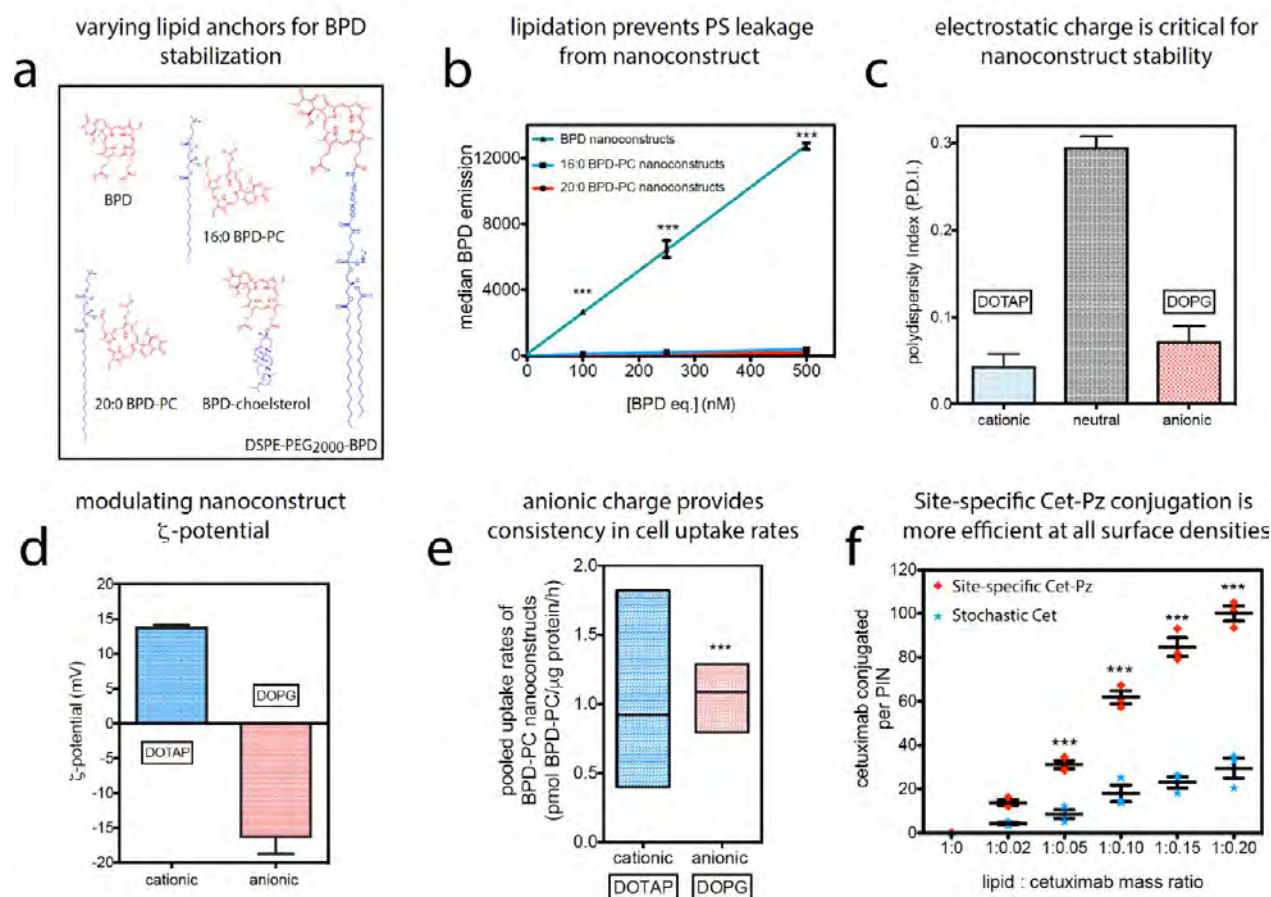


Figure 1. Varying lipid anchors for BPD stabilization: (a) chemical structures of BPD and its lipidated variants conjugated to cholesterol, 20:0 lyso PC, 16:0 lyso PC, and DSPE-PEG₂₀₀₀-NH₂ as anchors to promote membrane stability and eventually specificity when targeted with Cet. (b) Flow cytometry analysis reveals that the nanoconstructs formulated with 16:0 and 20:0 BPD-PC variants prevent non-specific PS leeching into OVCAR-5 cells, as compared to non-lipidated BPD nanoconstructs. Tuning nanoconstruct ζ -potential: (c) BPD-PC nanoconstructs doped with 0.5 mol % DSPE-PEG₂₀₀₀-DBCO for copper-free click conjugation to Cet aggregate in the absence of cationic DOTAP or anionic DOPG lipid dopants. (d) ζ -Potential of DOTAP and DOPG-containing BPD-PC nanoconstructs. (e) Min–max box plots of pooled BPD-PC nanoconstruct uptake rates in cancer cells expressing varying degrees of EGFR reveal that the anionic nanoconstructs have a favorable, lower variance in uptake rates before Cet conjugation (two-tailed *t* test, *F* test of variance). Tuning surface Cet grafting: (f) Degree of conjugation of site-specific Cet-Pz is more efficient than the conjugation of stochastic Cet at all the lipid:Cet mass ratios tested (mean \pm S.E., one-way ANOVA with a Tukey post-test; *n* = 3 for b, c, d, and f; *n* = 6 for each cell line \times rates from three cell lines pooled for each construct).

desmoplastic MIA PaCa-2 + PCAF tumors. In this first report of a specificity-tuned Cet-PIN for molecular targeted NIR photodynamic activation in desmoplastic heterotypic PDAC tumors, we show that treatment induces substantial tumor necrosis throughout the entirety of the tumor cross-section at an administered BPD equivalent dose that is 10-fold lower than the human equivalent dose required.⁷ Interestingly, molecular targeted NIR photodynamic activation also resulted in the photomodulation of tumor collagen, reducing the fractional collagen area by 1.5-fold.

The significance of this desmoplasia-modulating, molecular targeted NIR photodynamic activation approach lies in that it accelerates the conceptual shift in light-activation for drug delivery and therapeutic combinations. Recent work by our group^{9,11} and others^{41–43} demonstrated that combination therapies using light-activated nanoconstructs synergistically enhance efficacy. These, along with ongoing clinical efforts to introduce molecular specificity to chemotherapy-encapsulating nanomedicines for PDAC and other cancers (MM-310, Ephrin

A2 targeted liposomal docetaxel),⁴⁴ accentuate the high translational potential of our Cet-PINs. As a proof of concept, we also show that encapsulation of the front-line PDAC chemotherapeutics gemcitabine hydrochloride, 5-fluorouracil, and oxaliplatin, within the Cet-PINs, yields chemo-per-Cet payloads that are not achievable with direct antibody conjugates. We show that the Cet-PIN-Gemcitabine (41 chemo per Cet payload), the Cet-PIN-5-fluorouracil (1200 chemo per Cet payload), and the Cet-PIN-Oxaliplatin (20 chemo per Cet payload) all improve treatment response in heterotypic MIA PaCa-2 + PCAF organoids following photodynamic activation. They do so by combining photodynamic therapy with chemotherapy in a single construct at payloads that are not achievable in direct antibody conjugates without impairing binding specificity. The release of the entrapped, water-soluble agents is also regulated by NIR photochemical activation of the BPD-PC, as the presence of sodium azide can inhibit the release of calcein disodium salt, a fluorescent surrogate for entrapped chemotherapeutics (Figure S5f).

We here present a uniquely powerful modality with spatiotemporally controlled light-activable features, molecular specificity, and desmoplasia-modulating characteristics. Being a key critical barrier to drug delivery in PDAC, we envisage that the photomodulation of collagen by a single targeted nanoconjugate will also have a marked impact on subsequent Cet-PIN delivery for repeated cycles of NIR photodynamic activation.

With existing treatments currently falling short of providing effective control of PDAC progression, in addition to inducing significant dose-limiting comorbidities, there is a critical unmet need for a paradigm shift in therapeutic strategies. With the capacity to provide safer photodynamic illumination protocols and multiagent delivery, the integrated molecular targeted NIR photodynamic activation modality using specificity-tuned Cet-PINs that we present here is a significant stride forward in the pursuit for rationally designed treatments with improved patient outcomes.

Results and Discussion. Although a few prior examples of targeted photoactivable lipid-based nanomedicines have shown some promise *in vitro*, most have often failed to demonstrate more than two-fold selectivity of binding and phototoxicity, if at all.^{28–36} *In vivo*, little evidence exists in the literature that solid tumors can be effectively destroyed using such molecular targeted lipid-based constructs.³⁶ These failures underscore a fundamental, multiparametric complexity in developing and optimizing targeted photoactivable lipid-based nanomedicines, which have been generally overlooked and unaddressed in the literature. These complexities are either PDT-related, nanoconstruct-related, or combinations of both. Using the following systematic specificity-tuning process to engineer optimal Cet-PINs, we identify and modulate key nanoconstruct parameters to deliver the highest degrees of molecular specificity, tumor tissue penetration, and targeted photokilling in monotypic and heterotypic PDAC organoids and *in vivo* xenograft tumors.

Chemical Modulation of Benzoporphyrin Derivate Membrane Stability by Lipidation. In addition to the existing challenges facing the fabrication of ligand targeted nanoconstructs,⁴⁵ the NIR light-activable component of PINs introduces significant variability in the physicochemical properties of the plethora of promising clinical PSs available and variability in the stability within their nanoconstruct carriers. Here, we show that PS-nanoconstruct stability is non-trivial, yet it is of paramount importance for their molecular targeting specificity.^{28–34} One example of this variability is reported in our previous study, which shows that non-covalent antibody-associated liposomal BPD constructs exhibit some degree of binding specificity but suffer from substantial PS leakage as the extent of antibody adsorption increases.⁴⁶ Similarly, another study found that transferrin targeted liposomal hypericin was ineffective *in vivo* due to substantial leakage of the PS.³⁶ This relationship between PS hydrophobicity and liposomal association has also been a focal point of interest in the literature.⁴⁷ As such, we have adopted a lipid anchoring strategy for BPD to modulate its membrane stability and promote nanoconstruct integrity.⁴⁸ In this study, we found that BPD hydrophobically entrapped in a liposomal membrane rapidly and non-specifically leeches into OVCAR-5 cells that were used as a model high-EGFR expressing cell line, unlike a lipidated fluorophore (DSPE-Liss Rhod B) membrane anchored to the same construct (Figure S1a,b). Without the stable membrane insertion of BPD into the nanoconstruct, attempts at antibody targeted delivery of BPD become futile. Lipidic bilayered

nanovesicles formed of lipidated porphyrins, first reported in 2002,⁴⁹ have been previously prepared by the conjugation of porphyrins to phospholipid acyl chains,⁴⁹ glycerol moieties,^{48,50,51} phosphate head groups,^{52,53} and PEG chains.^{48,54} Recent studies by Zheng and Lovell have demonstrated the unique properties of lipidated porphyrin constituents of nanomedicines and nanotheranostics.^{43,50} We thus synthesized a panel of liposomal nanoformulations of BPD and its lipidated variants conjugated to 16:0 lyso PC, 20:0 lyso PC, and cholesterol through Steglich esterification or to DSPE-PEG₂₀₀₀-NH₂ by EDC-amide coupling.⁴⁸ Cholesterol was selected as a classical membrane anchor,⁵⁵ 16:0 lyso PC and 20 lyso PC were compared for their varying acyl chain length, and DSPE-PEG₂₀₀₀-NH₂ was selected for its double acyl chain membrane anchors. The chemical structures of BPD and its lipidated variants used in this study are shown in Figure 1a. Lipidation of BPD had no impact on its absorption properties, as determined by the lack of spectral shifts in the Soret or Q-band maxima of BPD (Figure S1c) or the Q-band full-width half maxima.⁴⁸ Our prior work has shown that the photochemistry of BPD is also not impaired following conjugation to lipids, making them suitable alternative NIR-photoactivable agents for the specificity-tuned constructs engineered here.⁴⁸ Conjugation of BPD to cholesterol resulted in the loss of its membrane-inserting properties and was not used further. DSPE-PEG₂₀₀₀-BPD nanoconstructs were unstable, exhibiting a polydispersity index (P.D.I.) greater than 0.2, possibly due to the terminal extension of the hydrophobic BPD molecules into the external aqueous phase. However, the 16:0 BPD-PC and 20:0 BPD-PC nanoconstructs remained colloidally stable with the BPD inserted into the hydrophobic bilayer (Figure S1d). When incubated with OVCAR-5 cells for 30 min, 16:0 and 20:0 BPD-PC nanoconstructs demonstrated no PS leaching at up to 500 μ M BPD equivalent and reduced non-specific uptake over 24 h (Figure 1b; Figure S1e). The 16:0 BPD-PC variant, referred to as BPD-PC from hereon, was selected for the remaining studies as its membrane stability was equal to that of the 20:0 PC variant and as its acyl chain length matched that of DPPC, the main phospholipid constituent used for the Cet-PINs. Nanoformulation of BPD-PC preserved 60% of the fluorescence and photodynamic activity of the hydrophobic PS in PBS, which was 21% greater than that of the BPD nanoconstructs (Figure S1f). This favorable opto-chemical superiority of the high-payload BPD-PC nanoconstructs is attributed to the steric prevention of BPD aggregates in the bilayer when lipidated and further motivated its selection as the PS variant for the specificity-tuned Cet-PINs.

Steric and Electrostatic Tuning To Regulate Specificity. To conjugate Cet site-specifically or stochastically to the PINs using bioorthogonal and chemoorthogonal copper-free click chemistry, a strained dibenzocyclooctyl (DBCO) moiety was needed at the BPD-PC nanoconstruct surface. However, DBCO functional groups are hydrophobic and promote nanoconstruct aggregation. The stability of BPD-PC nanoconstructs doped with a total of 5 mol % DSPE-PEG₂₀₀₀ was increasingly compromised by incorporating small amounts of DSPE-PEG₂₀₀₀-DBCO. BPD-PC nanoconstructs doped with 2 mol % DSPE-PEG₂₀₀₀-DBCO and 3 mol % DSPE-mPEG₂₀₀₀ were immediately unstable following extrusion (Figure S1h). Although the nanoconstructs with 1% DSPE-PEG₂₀₀₀-DBCO and 4% DSPE-mPEG₂₀₀₀ were stable following preparation, they precipitated overnight. Colloidal stability was only achieved at 0.5 mol % DSPE-PEG₂₀₀₀-DBCO doping when counter-

specificity of binding and targeted photodynamic therapy in 2D cultures

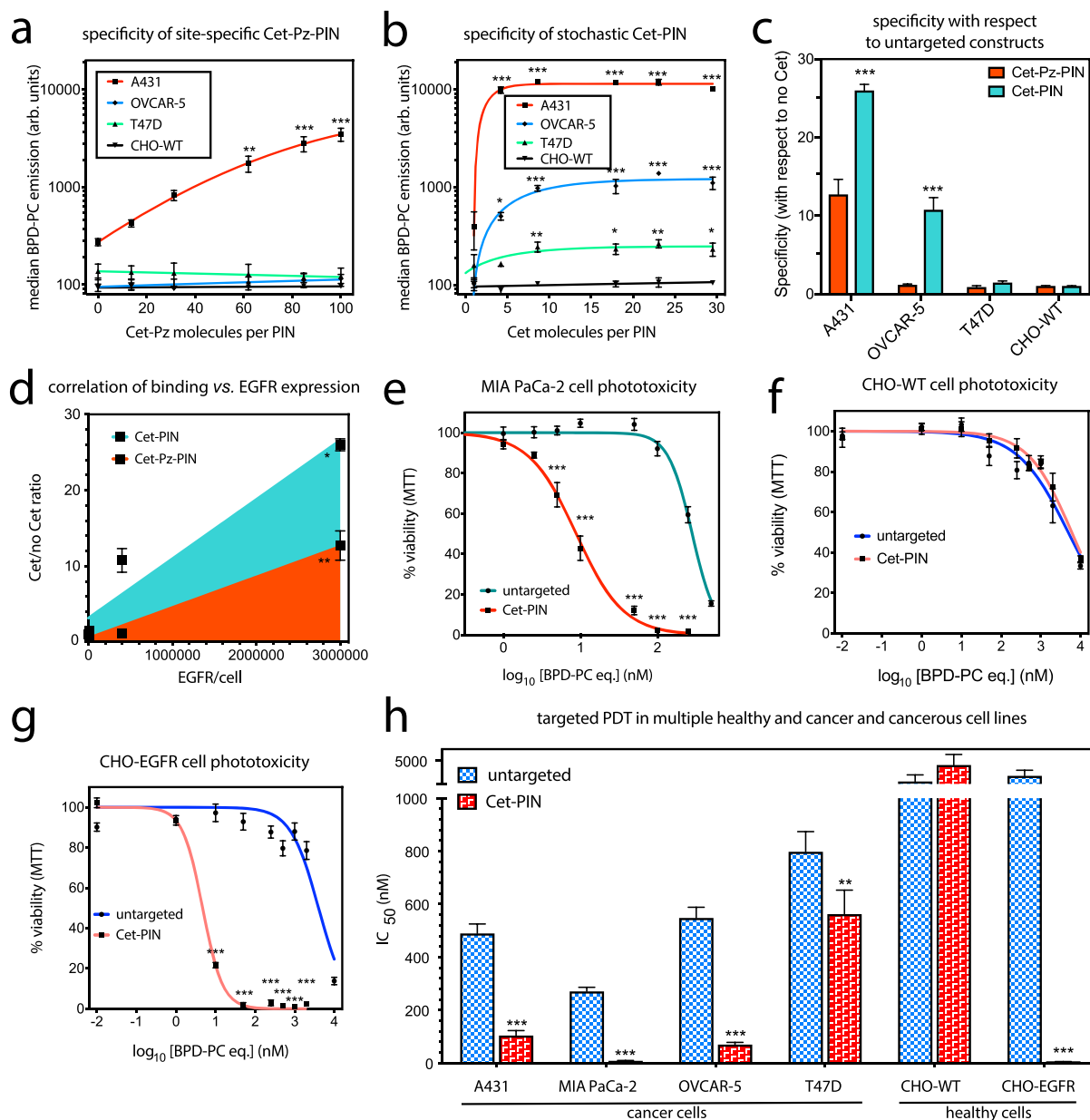


Figure 2. Binding of PINs conjugated to various densities of (a) site-specific Cet-Pz and (b) stochastic Cet to A431 ($2\text{--}4 \times 10^6$ EGFR/cell), OVCAR-5 (4×10^5 EGFR/cell), T47D (7×10^3 EGFR/cell), and CHO-WT (0 EGFR/cell) cell lines. (c) Binding specificity of the most efficient site-specific 100 Cet-Pz PINs and the stochastic 30 Cet-PINs is also presented with respect to the untargeted nanoconstructs (0 Cet per PIN molecule) for each cell line. (d) Pearson's r correlation between Cet-Pz-PIN and Cet-PIN binding, and cellular expression levels of EGFR revealed that the binding of both constructs positively correlates with EGFR expression, but the Cet-PIN binding is more efficient (mean \pm S.E., two-tailed t test). Representative phototoxicity dose-response curves of the untargeted construct and the specificity-tuned Cet-PIN in (e) MIA PaCa-2, (f) healthy CHO-WT, and (g) healthy CHO-EGFR cells demonstrate the EGFR-dependence of phototoxicity. (h) Molecular targeted phototoxicity was evaluated in a panel of cell lines expressing varying degrees of EGFR, and the differences in IC_{50} values between NIR photodestruction using untargeted constructs and the optimal specificity-tuned Cet-PINs are presented. The NIR photodynamic activation regimen used was 690 nm light irradiation with 20 J/cm^2 at 150 mW/cm^2 (mean \pm S.E.; $n = 3$ for a–d and $n = 8$ for e–h; one-way ANOVA with a Tukey post-test; *** = $P \leq 0.001$; ** = $P \leq 0.01$; * = $P \leq 0.05$).

stabilized with 4.5 mol % DSPE-mPEG₂₀₀₀ (Figure S1h). Not only was the modulation of DSPE-PEG₂₀₀₀-DBCO doping critical for stability, electrostatic repulsion of nanoconstructs was also needed and was achieved by the incorporation of 7.9 mol % of either DOTAP (cationic lipid) or DOPG (anionic lipid) (Figure 1c,d).

Electrostatic charge is a prime example of a biochemical PIN variable that has not been investigated in the context of antibody

targeting of nanoconstructs in general, let alone for NIR activable PINs. Electrostatics have long been assumed to play a binary role in nanoparticle delivery: cationic nanoparticles promote cell membrane association,⁵⁶ while anionic nanoparticles exhibit more favorable pharmacokinetics *in vivo*.⁵⁷ Here, we show that the tuning of electrostatic charge to an anionic ζ -potential plays a critical role in achieving consistent cellular interactions within a heterogeneous EGFR-expressing

population. We found that the electrostatic charge of the constructs influenced the intercellular variability of uptake rates before targeting between A431, OVCAR-5, and T47D cells that have varying degrees of EGFR expression (Figure S1i). Variability in intercellular uptake (prior to Cet conjugation) is a critical barrier for consistent cellular binding and uptake after targeting. This has negative consequences when attempting to maintain a consistent degree of specificity in heterogeneous tumor populations. The mean pooled cellular uptake rates of cationic and anionic BPD-PC nanoconstructs before targeting were similar; however, we found that the intercellular variance was significantly lower with the anionic DOPG-doped nanoconstructs (two-tailed unpaired *t* test, *F* test $P < 0.0001$, Figure 1e). Considering that the degree of variability in uptake rates of the anionic BPD nanoconstructs (prior to Cet conjugation) between the different cell lines tested was lower than that of the cationic nanoconstructs, the anionic constructs were selected as the platform for antibody conjugation and further PIN tuning and evaluation.

Modulating Antibody Orientation and Density of Surface Grafting Using Copper-Free Click Chemistry. Antibody targeting of nanoconstructs in general often suffers from complexities in conjugation that are centered around perturbative, inconsistent chemical coupling, and antibody disorientation.⁵⁸ Recent work has demonstrated the critical need for fine-tuning antibody targeted nanotherapeutics, as the molecular specificity can be markedly impaired when an one-size-fits all approach to nanoengineering is adopted.⁴⁵ To circumvent issues pertaining to structurally perturbative antibody conjugation techniques that are common to PINs, such as amine-sulfhydryl cross-linkers^{29,30,34} and thiol-maleimide chemistry,^{32,59,60} we adopted chemoorthogonal and bioorthogonal copper-free click chemistry^{61–66} to couple Cet to BPD-PC nanoconstructs. Following promising findings of an Fc-specific photo-cross-linked Protein Z (Pz) intermediary,^{67,68} we site-specifically conjugated Cet to BPD-PC nanoconstructs and compared their efficiencies with stochastically conjugated Cet constructs to determine the optimal antibody orientation for maximal PIN specificity.^{32,69–72}

Cet was site-specifically modified with an azido-Protein Z intermediary, photo-cross-linked to the Fc fragment (Cet-Pz), or stochastically modified with a single azido-PEG moiety (validated by Cy5-DBCO labeling; Figure S2a–c). At all lipid/Cet mass ratios greater than 1:0.05, site-specific conjugation of Cet-Pz was more efficient than stochastic conjugation of Cet, suggesting that the constant site-specific availability of the azido linker offers superior control over conjugation (Figure 1f).

As with other bioconjugate systems, the tendency for adsorption and non-covalent interactions compromises the integrity of the nanoconstructs in biological milieu and can impair molecular specificity. Thus, we validated the chemical conjugation of site-specific Cet-Pz and stochastic Cet to the nanoconstructs using two methods. The first was by preinactivating the nanoconstruct surface DBCO by incubation with 0.1 M sodium azide for 24 h (Figure S2d). Both stochastic and site-specific conjugation of Cet to DBCO-inactivated PINs were significantly decreased (Figure S2e,f). Second, the degree of non-covalent Cet adsorption was also assessed by incubating site-specific Cet-Pz and stochastic Cet with nanoconstructs containing non-reactive DSPE-PEG-NH₂ in place of the DBCO lipid. Cet adsorption was found to be negligible in both Cet preparations (Figure S2e,f).

Table S1 provides details of the full physical characterization of the site-specific Cet-Pz-PINs and stochastic Cet-PINs prepared, where the polydispersity indices of the Cet-Pz-PINs are greater than those of the Cet-PINs, suggesting a greater disparity in size distribution. However, the anionic charge is maintained in all PINs prepared, which is crucial to minimize variations in nanoconstruct–cell interactions at the various antibody surface densities tested.

Tuned Cellular Binding Specificity and Targeted Phototoxicity in 2D Monolayer Cultures. To tune the surface grafting of site-specific Cet-Pz (Figure 2a) and stochastic Cet (Figure 2b) to PINs, the binding specificity at different surface densities was measured in A431 ($(2–4) \times 10^6$ EGFR/cell),⁷³ OVCAR-5 (4×10^5 EGFR/cell),⁷⁴ T47D (7×10^3 EGFR/cell),⁷⁵ and CHO-WT (EGFR null)⁷⁶ cells using flow cytometry following a 30 min incubation period in serum-containing media at 37 °C. The most efficient Cet-Pz surface density was found to be 1129.1 ± 66.6 Cet-Pz per μm^2 , which equates to ~ 100 Cet-Pz molecules per PIN. This site-specific Cet-Pz-PIN exhibited 36.2-fold preferential binding to A431 cells over CHO-WT cells (Figures 2a and S3a). The most efficient stochastic Cet density was found to be only 517.5 ± 138.6 Cet per μm^2 , which equates to ~ 30 Cet molecules per PIN. Surprisingly, the stochastic Cet-PIN was found to exhibit unprecedented preferential binding specificities to A431 cells (97.3-fold), OVCAR-5 cells (10.5-fold), and T47D cells (2.2-fold), as compared to CHO-WT cells (Figures 2b and S3a). The site-specific or stochastic nanoconjugate demonstrating the highest specificity, ~ 100 Cet-Pz per PIN (referred to as **Cet-Pz-PIN** from hereon) or ~ 30 Cet per PIN (referred to as **Cet-PIN** from hereon), respectively, was used for the remainder of the studies. Although optimal specificity would ultimately confer the greatest degree of preference of PINs for high-EGFR-expressing cancer tissue over low-EGFR-expressing healthy tissue, the specificity of PINs can also be represented as the binding efficiencies to EGFR-expressing cells, with respect to untargeted constructs. As such, we have also compared the binding specificity of the Cet-Pz-PINs and the Cet-PINs (with respect to untargeted constructs) in A431 cells, OVCAR-5 cells, T47D cells, and CHO-WT cells. The highest degree of specificity of 26-fold with respect to untargeted constructs was found to be for the A431 cells when using the Cet-PIN formulation. Overall, we found that the binding of the Cet-Pz-PINs and the Cet-PINs correlated positively with the EGFR expression levels in all the cell lines tested (Figure 2d; Pearson's $r = 0.9918$ and $P = 0.0082$ for the Cet-Pz-PINs; $r = 0.9992$ and $P = 0.0008$ for the Cet-PINs). However, upon quantifying the area-under-the-curve of the correlation, the Cet-PINs were found to be 2.72-fold more efficient at EGFR binding than the Cet-Pz-PINs (1.50×10^{10} vs 4.74×10^9 , respectively). Furthermore, we found that targeting using the stochastic Cet-PIN increased the rates of cancer-cell specific (OVCAR-5) internalization in a manner that was dependent on the stochastic Cet surface density (Figure S6e). In addition to providing the highest degree of molecular specificity, the ~ 30 Cet surface density per PIN provided the highest rate of cellular internalization, expediting the uptake of the therapeutic photosensitizing entities. This optimal stochastic Cet-PIN was therefore used for all further molecular targeted NIR photodynamic activation studies.

To further authenticate the binding specificity of the optimal specificity-tuned Cet-PIN, binding to OVCAR-5 cells was competitively inhibited by the presence of free Cet at a 100-fold molar excess to the concentration of Cet conjugated to the PINs.

Free 100× Cet resulted in greater than 80% inhibition in cellular binding, whereas the presence of 100× molar excess of free Trastuzumab or human IgG sham had no inhibitory effect, thereby further confirming the true molecular specificity of the optimal specificity-tuned Cet-PINs (Figure S3c).

It was interesting to find that at all Cet densities, cancer cell binding of the optimal stochastic Cet-PIN was superior to the site-specific Cet-Pz-PIN, suggesting that the stochastic Cet orientation at the PIN surface may offer the conformational freedom with the potential for optimal EGFR epitope binding. The elegant Pz approach was leveraged here to achieve a tightly regulated conjugation with high yields (Figure 1f).⁶⁷ Despite its inferior conjugation efficiency, the stochastic conjugation, which is simpler and less expensive than the site-specific conjugation, was 2.72-fold more efficient. This further points to the complexity of conjugation of targeting moieties to nanoconstructs and the importance of the robust specificity tuning we perform here.

The efficacy of molecular targeted NIR photodynamic activation using the specificity-tuned Cet-PIN was then compared with an untargeted BPD-PC nanoconstruct in a panel of cell lines with varying degrees of EGFR expression using 690 nm NIR light irradiation at irradiance of 150 mW/cm² and a fluence of 20 J/cm². In the MIA PaCa-2 cells, targeting improved the efficacy of photodestruction by 32.7-fold, reducing the IC₅₀ from 271.4 nM to 9.3 nM (Figure 2e,f,g; Table S2). As an ultimate control, molecular targeted NIR photodynamic activation was tested in CHO-WT (EGFR-null) and CHO-EGFR cells stably transfected with full-length EGFR.⁷⁷ Cet-PINs did not reduce the IC₅₀ of photodestruction in CHO-WT cells, as compared to untargeted constructs, whereas a remarkable 688.5-fold reduction in IC₅₀ was observed with Cet-PINs in CHO-EGFR cells, reducing the IC₅₀ from 3717.7 nM to 5.4 nM (Figure 2e–h, Table S2). Similar EGFR-dependent trends of photodestruction were observed for A431, OVCAR-5, and T47D cells (Figure 2h; Figure S3; Table S2). Molecular targeted phototoxicity of the Cet-PINs was found to be significantly higher than that of Cet-Pz-PINs following NIR photodynamic activation, which is consistent with its superior binding efficiencies (Figure S 3d).

The findings of the 2D *in vitro* testing rigorously confirm that the specificity-tuned Cet-PINs mediate an EGFR-dependent, molecular targeted NIR photodynamic destruction of cancer cells. As is consistent with other antibody-targeted therapies, Cet-PINs and Cet-Pz-PINs were found to be internalized through the endolysosomal pathway and remained in lysosomes up to 24 h of incubation (Figure S4).^{29,78–81} It is worth noting that for all the PIN concentrations tested, no dark toxicity was observed (Figure S5), as is ideal for an NIR activable therapeutic nanosystem.

Heterotypic Binding Specificity and Penetration. In light of the evident complexity of optimal PIN preparation, a critical need also exists for disease-recapitulating *in vitro* high-throughput screening platforms to rapidly validate their specificity and ability to penetrate desmoplastic PDAC tumor tissue. 3D organoid tumor models have been previously used to evaluate liposome⁸² and nanoparticle penetration,^{83,84} PIC selectivity,⁸⁵ and evaluation of PDT-based treatment regimens.^{86–88}

This is the first report of the binding specificity, penetration, and targeted phototoxicity of specificity-tuned Cet-PINs in both monotypic and heterotypic MIA PaCa-2 PDAC organoids cultured in the presence of PCAFs.⁸⁹ The PCAFs are

interspersed throughout the heterotypic organoids 48 h after seeding and represent 52.8% of the organoid cell population (Figure 3c; 6.8% intensity thresholding and 3-infinity pixel inclusion). PCAFs are critical stromal partners that are responsible for desmoplasia, in addition to paracrine signaling that is involved in treatment resistance in PDAC. The desmoplastic reaction results in stromal matrix deposition that constitutes up to 90% of the total PDAC tumor volumes.^{3,4} Desmoplasia, as discussed earlier, is a critical barrier that often prevents the penetration of therapeutics through PDAC tumor tissue. Given that PCAFs are supportive of PDAC progression and treatment resistance, it is also important that the PCAF component of tumors is also simultaneously destroyed following molecular targeted NIR photodynamic activation. However, depletion of the stroma alone must be avoided, as it can promote tumor metastasis. Recent work has shown that cancer-associated fibroblasts significantly overexpress and upregulate EGFR upon activation by vicinal cancer cells, as compared to normal fibroblasts residing in healthy tissue.^{90,91} This makes the PCAFs viable targets for the Cet-PINs in addition to the EGFR-overexpressing PDAC cells. Considering that MIA-PaCa-2 cells express 1.7×10^5 EGFR/cell,⁹² we calculated the approximate EGFR expression of PCAF cells to be 3.5×10^4 EGFR/cell based on the relative receptor expression levels of the two cell lines (Figure S6a). This is consistent with the relative Cet-PIN binding efficiencies to the two cell lines (Figure S6b–d). Importantly, no statistically significant difference was observed between the Cet-PIN binding patterns and the respective EGFR expression patterns in the two cell lines (Figure S6d; one-way ANOVA with Tukey post-test), further validating the molecular specificity of the Cet-PINs.

Using two-photon microscopy, we assessed the penetration of the specificity-tuned Cet-PINs through monotypic and heterotypic MIA PaCa-2 organoids that include PCAFs, which are usually responsible for desmoplasia-limited drug penetration in PDAC. Cet-PINs tagged with Alexa Fluor 680 were incubated with the monotypic and heterotypic organoids for 1, 6, and 24 h. Representative images of the heterotypic MIA PaCa-2 + PCAF organoids reveal that the Cet-PINs tagged with Alexa Fluor 680 exhibit a considerably higher binding affinity for the organoids at all time points than the untargeted constructs (Figure 3a). Image analysis of the optical z-stacks using a brightfield mask revealed that the highest specificity of 12.5-fold and 16.9-fold was observed for the monotypic MIA PaCa-2 and heterotypic MIA PaCa-2 + PCAF organoids at 6 h of incubation, respectively (Figure 3b). At 50% optical sections through the organoid z-planes, we show that the Cet-PINs efficiently penetrated the organoids even at only 1 h of incubation. We then quantified the binding specificity of the Cet-PINs to the monotypic MIA PaCa-2 and heterotypic MIA PaCa-2 + PCAF organoids at 1 h, 6 h, and 24 h of incubation, with respect to untargeted construct controls. The three-dimensional distribution of Alexa Fluor 680 tagged Cet-PINs within the organoids was imaged using two photon microscopy, and 3D reconstructions of the Cet-PIN-bound organoids were generated (Figure 3d).

Molecular Targeted NIR Photodynamic Activation in Monotypic and Heterotypic PDAC Organoids. After 48 h of seeding, targeted NIR photodynamic activation experiments were performed using a 6 h incubation time, which was determined to result in maximal binding specificity and efficient Cet-PIN penetration in the monotypic and heterotypic PDAC organoids (Figure 4a). Considering that one of the motivating

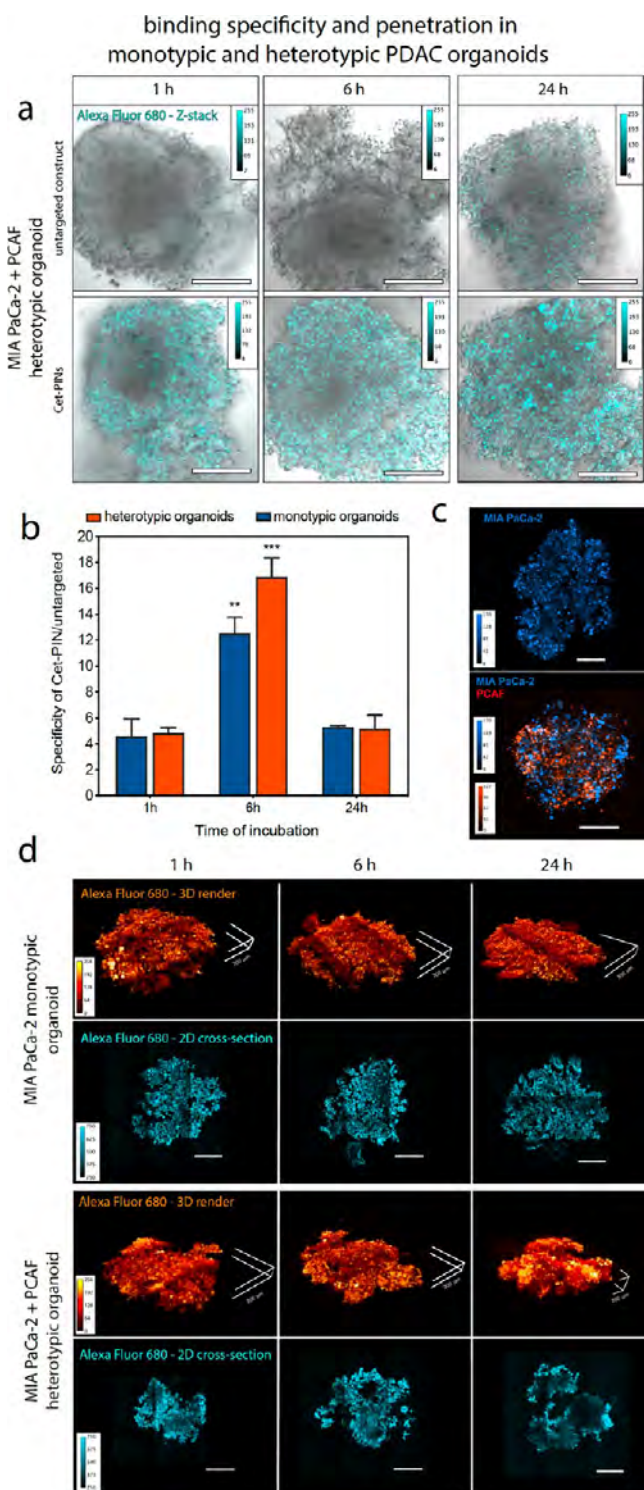


Figure 3. (a) Representative white light and sum-of-all-slices two-photon fluorescent image composites of heterotypic PDAC organoids at 1 h, 6 h, and 24 h incubation with untargeted constructs or Cet-PINs both labeled with Alexa Fluor 680. The organoids with the highest signals for each time point were used to establish the image acquisition parameters. (b) Organoid images were used to quantify the Cet-PIN binding specificity toward the monotypic and heterotypic PDAC organoids at 1 h, 6 h, and 24 h incubation, with respect to the untargeted construct. The highest specificity of Cet-PINs in both types of organoids was found to be at 6 h of incubation. (c) Characterization of spatial distribution of MIA PaCa-2 cells (blue, DiD labeled) in monotypic and heterotypic PDAC organoids containing PCAFs (orange; DiO labeled). (d) Two-photon images of Cet-PIN

Figure 3. continued

distribution throughout the monotypic and heterotypic PDAC organoids at 1 h, 6 h, and 24 h incubation. 3D renders of the PINs bound to the organoids are in orange and penetration in 2D cross-sections through 50% of the organoid's z-plane are shown in cyan, revealing efficient penetration through the organoids as early as 1 h incubation (scale bars in all images are 200 μm , specific 200 μm dimensions in (d) are highlighted, mean \pm S.E., one-way ANOVA with a Tukey post-test; *** = $P \leq 0.001$; ** = $P \leq 0.01$; significance with regards to respective organoids at all time points; $n = 3$ organoids per condition).

factors for developing such complex molecular targeted PINs for desmoplastic PDAC is to increase the payload of PS delivery in PDAC tissue, we compared the efficacy of high-payload delivery of the specificity-tuned Cet-PINs with lower-payload direct Cet-BPD photoimmunoconjugates (PICs)³⁹ and treated the organoids with them at equivalent Cet concentrations. The specificity-tuned Cet-PINs, untargeted constructs, and PICs were incubated for 6 h with increasing concentrations of BPD equivalent that were normalized to the concentration of Cet equivalent. The monotypic and heterotypic PDAC organoids were then irradiated with 40 J/cm² of 690 nm light at 150 mW/cm². Seventy-two hours following treatment, the LIVE/DEAD viability assay was performed on the organoids. The Comprehensive Image Analysis Procedure for Structurally complex Organotypic cultures (CALYPSO)⁸⁶ was used to generate viability heatmap images (Figure 4b; Figure S6g) and to quantify the fractional viability (Figure 4c) of the PDAC organoids. The IC₂₀ of NIR photodestruction using the Cet-PINs in the heterotypic MIA PaCa-2 + PCAF organoids was 105.4 nM BPD equivalent, which was almost identical to that of monotypic MIA PaCa-2 organoids (103.4 nM BPD equivalent). Furthermore, we found that the Cet-PINs improved the NIR photodestruction efficacy by reducing IC₂₀ values 16.8-fold in the monotypic MIA PaCa-2 organoids and 16.3-fold in the heterotypic MIA PaCa-2 + PCAF organoids, as compared to the untargeted construct (Figure 4c). The importance of these results lies in the fact that the specificity-tuned Cet-PINs were capable of circumventing any treatment resistance that is typically conferred by the presence of cancer-associated fibroblasts. It must be noted, however, that at the highest concentration of 2000 nM BPD equivalent, the mean heterotypic organoid viability was found to be 15.19% greater than the mean monotypic organoid viability. This is consistent with the residual viable cells that are observed following treatment with the highest concentration of 2000 nM BPD equivalent of Cet-PINs, which are not observed to the same extent in the monotypic organoids. Resistance to NIR photodynamic activation is a complex and multifaceted phenomenon. Factors that influence resistance in heterotypic three-dimensional organoids include microscale differences in light distribution and oxygen saturation, mechanistic cellular resistance to NIR photodynamic activation, PCAF activation status following treatment, and dynamic changes to EGFR expression in response to therapy. Understanding the mechanisms for the marginal residual disease following treatment in the heterotypic organoids is critical for designing appropriate dose-parameters for photodynamic activation and serve as the focus of future studies.

Importantly, we found that the PIC exerted no phototoxic effects on the monotypic and heterotypic PDAC organoids at

specificity-tuned Cet-PINs deliver high sensitizer payloads to PDAC organoids and facilitate multi-agent therapy

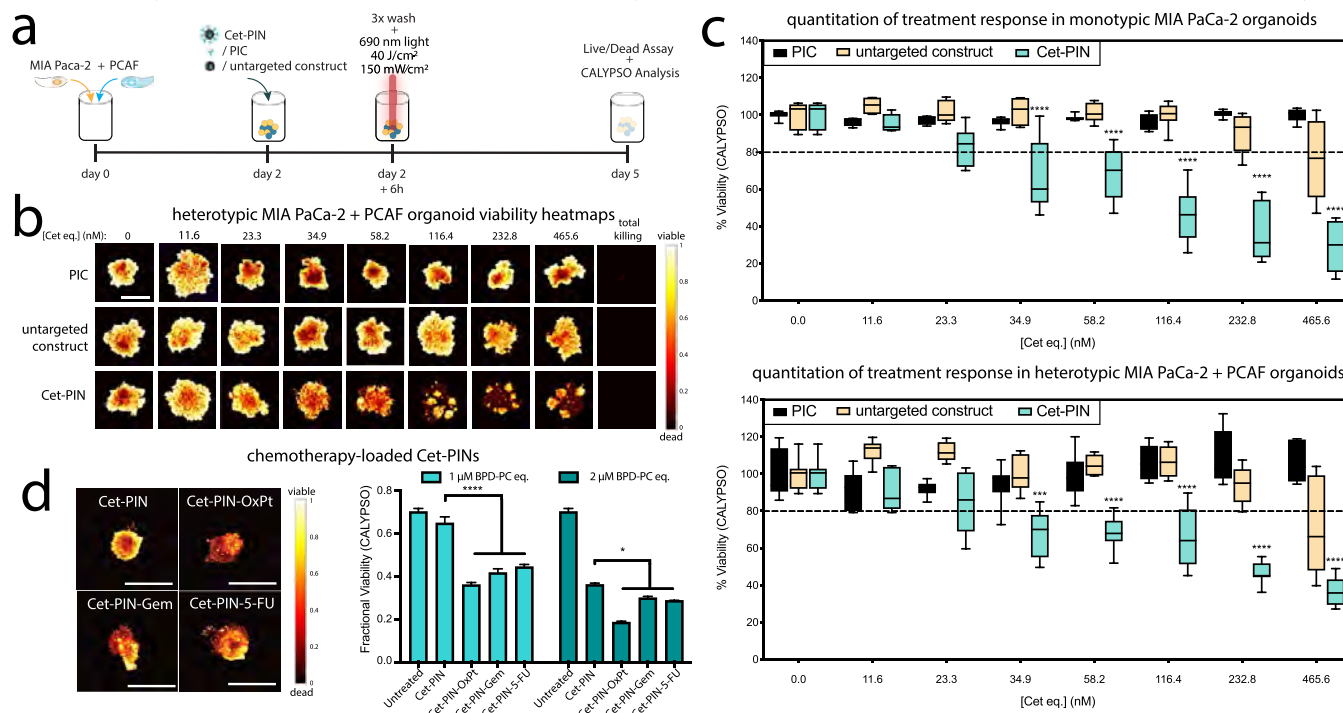


Figure 4. (a) Schematic representation of the culturing procedures and treatment regimen of monotypic and heterotypic PDAC organoids followed by imaging-based CALYPSO analysis of treatment response. (b) Viability heatmap images of heterotypic PDAC organoids following molecular targeted NIR photodynamic activation with increasing concentrations of PIC, untargeted construct, and the specificity-tuned Cet-PIN. (c) CALYPSO image analysis framework was used for the quantitation of monotypic and heterotypic PDAC organoid fractional viability following molecular targeted NIR photodynamic activation, comparing both monotypic and heterotypic PDAC organoids treated using the PIC, an untargeted construct and the specificity-tuned Cet-PIN. (d) Heterotypic PDAC organoids treated using Cet-PINs, Cet-PIN-OxPt, Cet-PIN-Gem, and Cet-PIN-5-FU with NIR photodynamic activation. The NIR photodynamic activation regimen used was 690 nm light irradiation with 40 J/cm² at 150 mW/cm² (scale bars are 1 mm, box plots with min–max data presentation, one-way ANOVA with a Tukey post-test for PIC and Cet-PIN, * = $P \leq 0.05$, *** = $P \leq 0.001$, **** = $P \leq 0.0001$; mean \pm S.E.M., $n = 4$ –8 organoids per condition).

the Cet concentration equivalents used in this study, and as such, no IC₂₀ values were derived. The PIC represents the current state of the art for molecular targeted photodynamic activation in the clinic,⁹³ and due to its limited payload efficiency, the treatment will remain mostly as a monotherapy. To exemplify the multifunctionality of our Cet-PIN platforms, the PDAC front line chemotherapeutics oxaliplatin, gemcitabine hydrochloride, and 5-fluorouracil were entrapped within the specificity tuned Cet-PINs (Cet-PIN-OxPt, Cet-PIN-Gem, and Cet-PIN-5-FU, respectively). The chemotherapy loaded Cet-PINs all provide Cet payloads that are not achievable with direct antibody conjugates, especially with regard to PICs that are already modified with up to eight PS molecules (Cet-PIN-OxPt, 20 molecules per Cet payload; Cet-PIN-Gem, 41 molecules per Cet payload; Cet-PIN-5-FU, 1200 molecules per Cet payload). Following incubation and NIR photodynamic activation within the heterotypic PDAC organoids, the Cet-PIN-OxPt, Cet-PIN-Gem, and Cet-PIN-5-FU all significantly increased the antitumor efficacy of the treatment, with respect to the chemotherapy-free Cet-PINs at both 1 μM and 2 μM BPD-PC equivalent of nanoconstructs (Figure 4d).

Our findings underscore the value of using such high-payload PINs with the amenability for multimodal therapy, given that their biochemical tuning is diligent and rigorous to confer both sufficient tumor organoid tissue penetration and optimal binding specificity.

In Vivo Molecular Targeted NIR Photodynamic Activation of Desmoplastic Heterotypic PDAC Tumors. As the ultimate utility of our tuned Cet-PINs is for *in vivo* NIR photodynamic activation regimens, we performed acute *in vivo* evaluation of the perivascular penetration and molecular targeted NIR photo-destruction of desmoplastic PDAC using the specificity-tuned Cet-PINs, as outlined in Figure 5a. In a subcutaneous heterotypic murine xenograft model of pancreatic cancer consisting of MIA PaCa-2 and PCAF cells, we first quantified the degree of Cet-PIN tumor penetration using photoacoustic imaging. The tumors were imaged prior to the administration of the Cet-PIN labeled with IRDye800CW (Cet-PIN-IRDye800) to generate 2D and 3D baseline mapping of tumor blood vessels and imaged again 12 h after intravenous administration of the Cet-PIN-IRDye800 to generate 2D and 3D mapping of the tumoral distribution of the construct (Figure 5b). The validity of the photoacoustic signals arising from the Cet-PIN-IRDye800 was confirmed by quantitation of the photoacoustic tumor images before and after administration (Figure 5c). Using 15 randomly selected vessels from 2D cross-sectional images from three different mice, the perivascular distance of Cet-PIN penetration was quantified and found to range from 174–473 μm (Figure 5d).

To evaluate the efficacy of the specificity-tuned Cet-PINs in desmoplastic PDAC tumors *in vivo*, we administered 0.5 mg/kg BPD equivalent of the constructs into mice bearing MIA PaCa-2 + PCAF xenograft tumors. Notably, this administered dose is

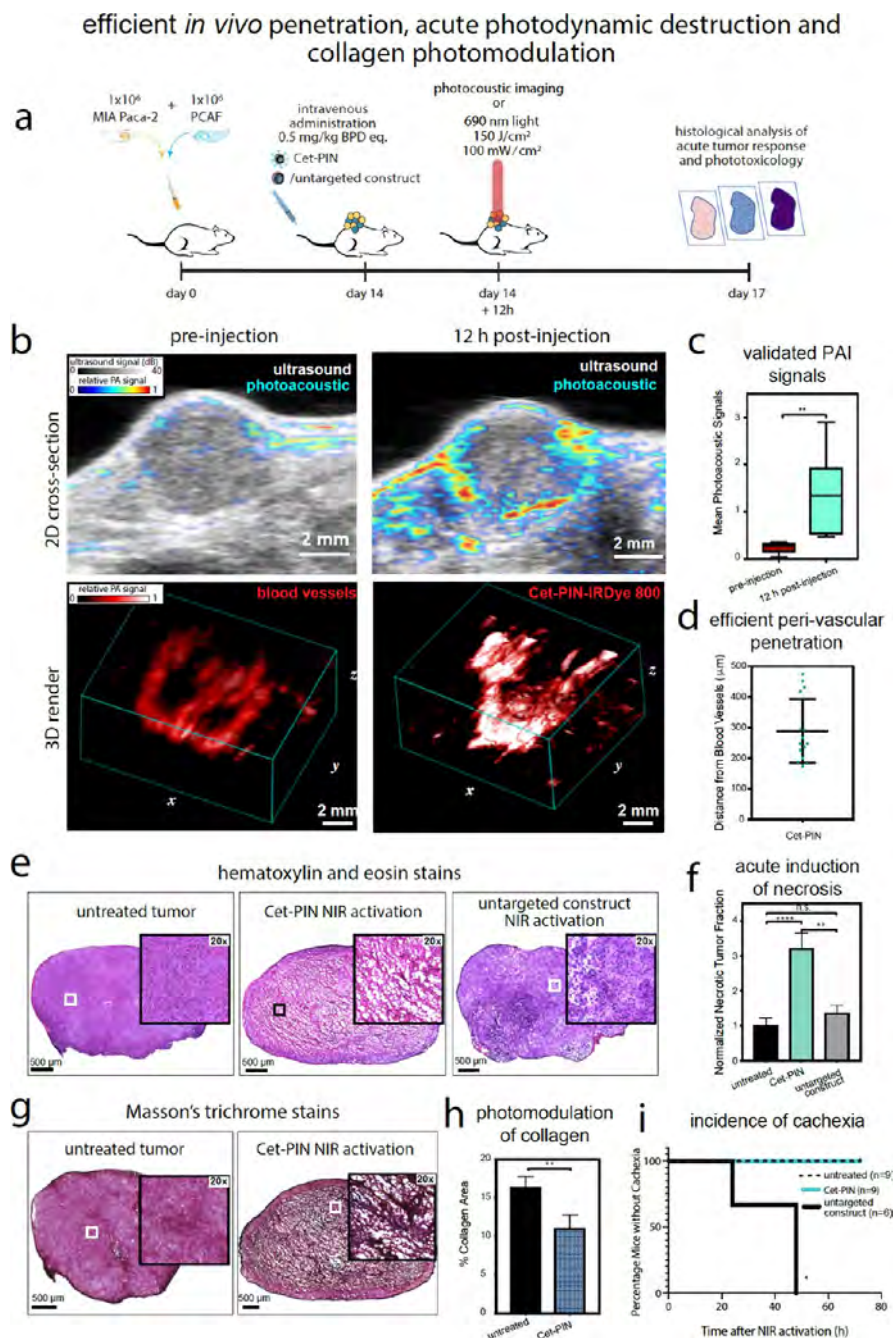


Figure 5. (a) Schematic representation of the time-scale of *in vivo* heterotypic tumor implantation, Cet-PIN administration, photoacoustic imaging, or molecular targeted NIR photodynamic activation and histological analyses of tumor responses to therapy. (b) Two-dimensional cross-sections and three-dimensional renders of heterotypic MIA PaCa-2 + PCAF tumors *in vivo* before and after intravenous administration of the Cet-PIN tagged with the photoacoustic contrast agent IRDye800CW (Cet-PIN-IRDye800). (c) Quantitation of photoacoustic signals before and after intravenous administration of the Cet-PIN-IRDye800 validates that the detected photoacoustic signal is arising from the administered construct. (d) Quantitation of perivascular tumor penetration of the Cet-PIN-IRDye800 shows that the constructs exhibit efficient tumor penetration *in vivo*. (e) HE stains of untreated tumors and tumors treated with NIR photodynamic activation of the Cet-PIN or the untargeted constructs. Significant necrosis throughout the tumor cross-section is only observed in the tumors treated with the Cet-PIN at 72 h following therapy. (f) Quantitation of HE images in (e) reveals a significant increase in necrotic area following NIR photodynamic activation using the Cet-PIN, which is not the case following NIR photodynamic activation of tumors in mice treated with the untargeted construct. (g) Masson's trichrome stains of tumor sections with and without NIR photodynamic activation using the Cet-PIN reveal a significant reduction in collagen content (blue), following therapy. This is quantified in (h). (i) Incidence of acute mouse cachexia during the 72 h following treatment. Cachexia was observed in 100% of mice 72 h following NIR photodynamic activation of untargeted constructs, whereas untreated mice and mice treated with NIR photodynamic activation of Cet-PINs remained healthy (means \pm S.E., two-tailed *t* test, ** = $P \leq 0.01$; $n = 3$ mice \times 3 z-planes for b and c; $n = 6$ mice \times 6 slices per tumor for e and f, $n = 3$ mice (9 total untreated tumor slices) in g and h; $n = 4$ mice (8 total PDT-treated tumor slices) in g and h; Logrank test, ** = $P < 0.05$, $n = 6-9$ in d).

\sim 10-fold lower than the Visudyne dose administered to patients undergoing PDT for PDAC, underscoring the efficiency of

molecular targeted PS delivery with our specificity-tuned Cet-PIN formulation.⁷ This further highlights the power of

intelligently engineering high-payload photonanomedicine systems to reduce the adverse effects associated with high PS administrations. NIR photodynamic activation was performed 12 h following intravenous administration of the Cet-PINs. Seventy-two hours following *in vivo* molecular targeted NIR photodynamic activation, the heterotypic PDAC tumors were harvested, sectioned, and stained using hematoxylin and eosin (HE) to evaluate tissue necrosis and Masson's Trichrome stain to evaluate the collagen content in the tumors with and without therapy. It was found that only molecular targeted NIR photodynamic activation induced substantial necrosis throughout the entire cross-section of the tumors, as treatment using the untargeted constructs failed to induce significant tumor necrosis (Figure 5e). This was also quantified using image analysis, showing a statistically significant ~3-fold increase in fractional necrotic area 72 h following molecular targeted NIR photodynamic activation, with a negligible and non-statistically significant increase in necrosis following treatment using the untargeted constructs (Figure 5f).

Of considerable significance, we show that molecular targeted NIR photodynamic activation using the specificity-tuned Cet-PINs directly reduced the density of tumor collagen by 1.5-fold (Figure 5g,h; blue). The photomodulation of tumor collagen, which is produced by the activated PCAF cells within the tumor, is of paramount importance, as it demonstrates the potential for using our optimized Cet-PIN and NIR photodynamic activation to improve the tumor delivery and permeability of Cet-PINs during repeated treatment cycles that are known to be significantly limited by desmoplastic tumor stroma.

Molecular targeting of nanomedicines has also been reported to increase the antitumor efficacy of anticancer treatments, and thus, we have shown this to be the case for the Cet-PINs here. However, the ultimate goal of molecular targeting of such high-payload systems such as the Cet-PINs we present here is to allow for expansive and unrestricted illumination protocols during photodynamic treatment of *in vivo* pancreatic tumors. This is achieved by restricting phototoxicity to the receptor-over-expressing tumor tissue, thereby maximizing the safety of the illumination protocol. With regards to the molecular specificity of photodamage induced by NIR photodynamic activation of the Cet-PINs, we show that treatment of low EGFR-expressing T47D tumors using Cet-PINs did not significantly increase tumor necrosis (Figure S6d). In addition, there was no significant difference in fractional tumor necrosis between treatment using the Cet-PINs and the untargeted constructs. As improving the safety of photodynamic therapy protocols using molecular targeting is the priority, we evaluated the health of the mice following NIR photodynamic activation with either the Cet-PINs or untargeted constructs.

Within 72 h following NIR photodynamic activation in mice administered with untargeted constructs, all mice had developed severe cachexia and moribundity (Figure S7a), whereas all mice treated with Cet-PINs remained healthy following NIR photodynamic activation (Figure 5i). Mice treated with untargeted constructs also exhibited significant acute weight loss from as early as 48 h following NIR photodynamic activation, whereas mice treated with Cet-PINs experienced no change in body mass following NIR photodynamic activation (Figure S7b). The most common cause of toxicity in patients undergoing PDT within the vicinity of the peritoneum is bowel perforation.⁹⁴ As is consistent with the clinical observations, we found that the mice with cachexia following treatment with untargeted constructs had visible signs of bowel photodamage

and ulceration, in addition to bowel perforation that is visible in histological tissue sections (Figure S7c). Unlike treatment with the Cet-PINs, in the mice treated with untargeted constructs, there was substantial blistering in the skin covering the irradiated tumor, which was corroborated by necrosis in the epidermis that was visualized using HE staining (Figure S8). Furthermore, the muscle tissue surrounding the tumor that was also exposed to the NIR irradiation following administration of untargeted constructs exhibited visible signs of bruising, with one instance of a mouse losing function of the respective limb. HE staining of sections of vicinal muscle surrounding the irradiated tumors also showed significant necrosis and tissue damage following treatment using untargeted constructs. Liver segments beneath the irradiated tumors, however, appeared mostly unaffected. Unlike treatment using the untargeted constructs in this study in addition to untargeted BPD nanoformulations previously reported,⁹⁵ only very mild erythema in the skin directly illuminated with NIR light was observed, which was resolved within 3 days. As such, our study concludes that molecular targeting using the specificity tuned Cet-PINs preserved the health of the mice, protected them from any signs of toxicity, morbidity, or moribundity, and spared all off-target tissue from non-specific phototoxicity, all while concomitantly improving anti-tumor efficacy.

Conclusions. The dismal nature of PDAC therapy is attributed to a number of limiting factors including drug delivery and microenvironmental effects. While there is no shortage of highly potent, and likewise toxic, therapeutic agents to treat PDAC, systemic and dose-limiting toxicities in up to 40% of patients frequently result in termination of treatment.⁹⁶ As such, there is a critical need for a distinct treatment modality that addresses these limitations, in addition to providing direct, controlled damage to the tumor. PDT is an example of such a distinctive modality, whereby photodynamic activation results in photodynamic priming of the tumor, improving delivery and sensitizing the tumor to subsequent combination therapies.

Our study presents a unique demonstration of how a single, specificity-tuned photoimmunonanoconjugate (PIN) offers a distinct NIR-activable therapeutic regimen for desmoplastic PDAC with unprecedented molecular specificities of binding and targeted phototoxicities. Using a single clinically inspired nanoconjugate rigorously tuned for optimal specificity, we present the simultaneous EGFR molecular targeted photodynamic tumor destruction and photomodulation of tumor collagen. Considering that there is no shortage of toxic PDAC agents, the power of the PIN approach does not lie solely in its capacity to destroy tumor tissue. Improving the efficacy of targeted photosensitizer conjugates, such as low-payload photoimmunonanoconjugates (PICs), can be achieved by tethering to charged polymers and polymeric nanoparticles.^{97–100} However, the value of the PIN approach we present here lies in its capacity to integrate the following important facets in a single construct and a single treatment application: high-payload photosensitizer delivery, multiagent entrapment for multimodal therapy, molecular specificity, spatiotemporal control over photoinduced tumor necrosis, and photomodulatory effects of the desmoplastic tumor stroma. Furthermore, it is evident that NIR photodynamic activation of the specificity-tuned PINs *in vivo* results in previously unreported photomodulatory effects in desmoplastic PDAC tumors, which has implications in alleviating stroma-induced treatment resistance.

Given that PDAC is particularly challenging to treat due to the dense stromal deposition arising from activated PCAFs, the high

throughput *in vitro* screening models used must be appropriate to recapitulate elements of these stromal barriers. Motivated by this necessity, we developed heterotypic PDAC organoids that contain MIA PaCa-2 cancer cells and patient-derived PCAF cells in this study. Using this platform, we evaluated our high payload BPD-entrapping, specificity-tuned Cet-PINs. We show that the Cet-PINs rapidly penetrate the heterotypic PDAC organoids in under 1 h, exhibit binding specificities of up to ~16.9-fold, and improve molecular targeted NIR photodynamic killing efficacy by up to ~16-fold. Cet-PINs, encapsulated with the front-line PDAC chemotherapeutics oxaliplatin, gemcitabine hydrochloride, and 5-fluorouracil, further improved the antitumor efficacy in the heterotypic PDAC organoids, demonstrating a clear technical advance as compared to PICs.

For the first time, we here show that specificity-tuned Cet-PINs provide molecular targeted NIR photodynamic activation with excellent efficiencies of photodestruction in desmoplastic heterotypic PDAC tumors *in vivo* using a photosensitizer dose-equivalent that is 10-fold lower than the human equivalent dose needed for inducing effective PDAC necrosis in the clinic. At Cet-PIN doses and NIR light doses capable of inducing substantial PDAC tumor necrosis, vicinal healthy muscle tissue and skin covering the tumor that was exposed to the NIR beam were entirely unaffected. Conversely, equivalent doses of untargeted construct and NIR photodynamic activation were not capable of inducing similar tumor photodamage but did induce severe necrosis of the overlying skin, proximal muscle, and underlying bowel tissue that became perforated. Unlike the Cet-PINs, the untargeted constructs induced extreme weight loss, moribundity and cachexia in all treated mice. The findings we present here are the first to emphasize the criticality of imparting molecular specificity for light-activable nanomedicines. This ultimately allows for increased tolerability to photodynamic activation, allowing the field to move forward from the current accomplishment of controlled zones of tumor necrosis in patients, toward expansive curative illumination protocols that also spare healthy pancreatic tissue and vasculature. Furthermore, molecular targeted NIR photodynamic activation resulted in photomodulation of the desmoplastic tumor stroma, significantly reducing tumor collagen by 1.5-fold. The benefits of the treatment regimen provided by a single nanoconstruct with a single NIR photodynamic activation process have significant implications in targeted drug delivery, whereby photomodulation of collagen can improve PDAC response to subsequent rounds of treatment. By modulating the tumor biology to provide favorable microenvironments, photodynamic priming using specificity-tuned PINs paves the way for critically needed multimodal therapies in the pursuit of paradigm-shifting PDAC treatment regimens. The findings we present here warrant critical further investigation into the molecular basis for the photomodulation of desmoplastic collagen within the heterotypic PDAC tumors provided by NIR photodynamic activation of the specificity-tuned Cet-PIN. Future avenues of investigation include elucidating the effect of NIR photodynamic activation on the photooxidation of collagen, collagen order and tortuosity, desmoplastic tumor elasticity, autocrine and paracrine signaling pathways in PDAC and PCAF cells, and the PCAF activation status following treatment.

PDACs are also characterized by high rates of KRAS mutations (70–90%), rendering them resistant to Cet (Erbix) therapy for EGFR blockade,¹⁰¹ irrespective of the high rates of EGFR expression in patients with PDAC (85%).³⁷ This has led

to the failure of Cet (Erbix) as part of a combination treatment for PDAC. As such, Cet is currently used for clinical tumor imaging only.³⁸ Our prior work has shown that photodynamic priming of KRAS mutant ovarian cancers resensitizes the tumor cells to EGFR blockade using Cet, making the synergistic outcome superior to single treatments, which are both minimal and modest.¹⁰² With the capacity to also prime KRAS mutant PDAC cells for EGFR blockade using Cet, photodynamic priming by the NIR photoactivation of the specificity-tuned Cet-PIN is also expected to exert molecular synergy in the most resistant of PDAC subtypes, further enhancing outcomes.

This study forms the basis of integrating multimodal mechanistically inspired combination therapies within the Cet-PIN framework to reduce the toxicities associated with current PDAC treatments and high PS doses, to enhance their delivery to desmoplastic tumors, and to promote synergistic, spatiotemporally controlled therapies. These strategies that are designed to simultaneously mitigate multiple hurdles to effective PDAC management promise to push current clinical PDT regimens toward more complete, curative NIR-activated photodynamic treatment protocols while sparing healthy vicinal tissue and organ function to extend patient survival and maximize patient quality of life.

■ ASSOCIATED CONTENT

📄 Supporting Information

The Supporting Information is available free of charge on the ACS Publications website at DOI: [10.1021/acs.nanolett.9b00859](https://doi.org/10.1021/acs.nanolett.9b00859).

Materials and methods with supplementary results (PDF)

■ AUTHOR INFORMATION

Corresponding Author

*E-mail: thasan@mgh.harvard.edu.

ORCID

Girgis Obaid: [0000-0002-9452-4467](https://orcid.org/0000-0002-9452-4467)

Present Address

[†]Department of Biomedical Engineering, Tufts University, Medford, Massachusetts, 02155, United States.

Funding

Financial support was provided by the National Institutes of Health Grant Nos. P01CA084203, R01CA156177, R01CA160998, R21CA220143, and S10OD012326 to T.H. and K99CA215301 to G.O. We also gratefully acknowledge the Bullock-Wellman Fellowship to G.O. and the IIRSIP Fellowship from the Higher Education Commission (HEC) of Pakistan to S.B.

Notes

The authors declare no competing financial interest.

■ ACKNOWLEDGMENTS

We thank Drs. Danian Cao, Jie Zhao, Brijesh Bhayana, James Hui, and Ahmed Alkhateeb for their technical assistance and Drs. Bryan Spring, Sriram Anbil, Imran Rizvi, Akilan Palanisami, and Huang-Chiao Huang for insightful discussions. We also thank Dr. Andrew Tsourkas for providing the bacterial Protein Z expression cultures and DNA plasmid vectors.

■ ABBREVIATIONS

PINs, photoimmunonanoconjugates; BPD, benzoporphyrin derivative; BPD-PC, 16:0 lysophosphocholine BPD conjugate;

TLC, thin layer chromatography; NIR, near-infrared; Cet, cetuximab; PCAF, pancreatic cancer-associated fibroblasts; Pz, protein Z

REFERENCES

- (1) Conroy, T.; Desseigne, F.; Ychou, M.; Bouche, O.; Guimbaud, R.; Becouarn, Y.; Adenis, A.; Raoul, J. L.;ourgou-Bourgade, S.; de la Fouchardiere, C.; Bennouna, J.; Bacht, J. B.; Khemissa-Akouz, F.; Pere-Verge, D.; Delbaldo, C.; Assenat, E.; Chauffert, B.; Michel, P.; Montoto-Grillot, C.; Ducreux, M. Groupe Tumeurs Digestives of, U; Intergroup, P. *N. Engl. J. Med.* **2011**, *364* (19), 1817–25.
- (2) Ryan, D. P.; Hong, T. S.; Bardeesy, N. *N. Engl. J. Med.* **2014**, *371* (22), 2140–1.
- (3) Bolm, L.; Cigolla, S.; Wittel, U. A.; Hopt, U. T.; Keck, T.; Rades, D.; Bronsert, P.; Wellner, U. F. *Transl. Oncol.* **2017**, *10* (4), 578–588.
- (4) Waghray, M.; Yalamanchili, M.; di Magliano, M. P.; Simeone, D. *M. Curr. Opin. Gastroenterol.* **2013**, *29* (5), 537–43.
- (5) Weniger, M.; Honselmann, K. C.; Liss, A. S. The Extracellular Matrix and Pancreatic Cancer: A Complex Relationship. *Cancers* **2018**, *10* (9), 316.
- (6) Neesse, A.; Michl, P.; Frese, K. K.; Feig, C.; Cook, N.; Jacobetz, M. A.; Lolkema, M. P.; Buchholz, M.; Olive, K. P.; Gress, T. M.; Tuveson, D. A. *Gut* **2011**, *60* (6), 861–8.
- (7) Huggett, M. T.; Jermyn, M.; Gillams, A.; Illing, R.; Mosse, S.; Novelli, M.; Kent, E.; Bown, S. G.; Hasan, T.; Pogue, B. W.; Pereira, S. P. *Br. J. Cancer* **2014**, *110* (7), 1698–704.
- (8) DeWitt, J. M.; Sandrasegaran, K.; O'Neil, B.; House, M. G.; Zyromski, N. J.; Sehdev, A.; Perkins, S. M.; Flynn, J.; McCranor, L.; Shahda, S. *Gastrointest. Endosc.* **2019**, *89* (2), 390–398.
- (9) Spring, B. Q.; Bryan Sears, R.; Zheng, L. Z.; Mai, Z.; Watanabe, R.; Sherwood, M. E.; Schoenfeld, D. A.; Pogue, B. W.; Pereira, S. P.; Villa, E.; Hasan, T. *Nat. Nanotechnol.* **2016**, *11* (4), 378–87.
- (10) Celli, J. P.; Solban, N.; Liang, A.; Pereira, S. P.; Hasan, T. *Lasers Surg. Med.* **2011**, *43* (7), 565–74.
- (11) Huang, H. C.; Rizvi, I.; Liu, J.; Anbil, S.; Kalra, A.; Lee, H.; Baglo, Y.; Paz, N.; Hayden, D.; Pereira, S.; Pogue, B. W.; Fitzgerald, J.; Hasan, T. *Cancer Res.* **2018**, *78* (2), 558–571.
- (12) Snyder, J. W.; Greco, W. R.; Bellnier, D. A.; Vaughan, L.; Henderson, B. W. *Cancer Res.* **2003**, *63* (23), 8126–31.
- (13) Kobayashi, H.; Choyke, P. L. *Nanoscale* **2016**, *8* (25), 12504–9.
- (14) Bown, S. G.; Rogowska, A. Z.; Whitelaw, D. E.; Lees, W. R.; Lovat, L. B.; Ripley, P.; Jones, L.; Wyld, P.; Gillams, A.; Hatfield, A. W. *Gut* **2002**, *50* (4), 549–57.
- (15) Visudyne. *Control number: 189192 Product Monograph*; Novartis Pharmaceuticals Canada Inc.
- (16) NX Development Corp. (NXDC) Launches FDA-Approved Gleolan (aminolevulinic acid HCl) for Enhanced Visualization of High-Grade Gliomas (including Glioblastomas). *NX Development Corp Briefing Package*; NXDC, **2018**
- (17) Spring, B. Q.; Abu-Yousif, A. O.; Palanisami, A.; Rizvi, I.; Zheng, X.; Mai, Z.; Anbil, S.; Sears, R. B.; Mensah, L. B.; Goldschmidt, R.; Erdem, S. S.; Oliva, E.; Hasan, T. *Proc. Natl. Acad. Sci. U. S. A.* **2014**, *111* (10), E933–42.
- (18) Min, Y.; Caster, J. M.; Eblan, M. J.; Wang, A. Z. *Chem. Rev.* **2015**, *115* (19), 11147–90.
- (19) Obaid, G.; Broekgaarden, M.; Bulin, A. L.; Huang, H. C.; Kuriakose, J.; Liu, J.; Hasan, T. *Nanoscale* **2016**, *8* (25), 12471–503.
- (20) Tian, X.; Lind, K. R.; Yuan, B.; Shaw, S.; Siemianowski, O.; Cademartiri, L. *Adv. Mater.* **2017**, *29* (17), 1604681.
- (21) Lismont, M.; Dreesen, L.; Wuttke, S. *Adv. Funct. Mater.* **2017**, *27* (14), 1606314.
- (22) Freund, R.; Lächelt, U.; Gruber, T.; Rühle, B.; Wuttke, S. *ACS Nano* **2018**, *12* (3), 2094–2105.
- (23) Oliveira-Cunha, M.; Newman, W. G.; Siriwardena, A. K. *Cancers* **2011**, *3* (2), 1513–26.
- (24) (a) ClinicalTrials.gov Identifier: NCT03563248, Losartan and Nivolumab in Combination With FOLFIRINOX and SBRT in Localized Pancreatic Cancer. *Clinicaltrials.gov*; U.S. National Library of Medicine, 2019. <http://www.clinicaltrials.gov> (accessed September 19, 2019). (b) ClinicalTrials.gov Identifier: NCT03825289, Trametinib and Hydroxychloroquine in Treating Patients With Pancreatic Cancer (THREAD). *Clinicaltrials.gov*; U.S. National Library of Medicine, 2019. <http://www.clinicaltrials.gov> (accessed September 19, 2019). (c) ClinicalTrials.gov Identifier: NCT03634332, Second-line Study of PEGPH20 and Pembro for HA High Metastatic PDAC. *Clinicaltrials.gov*; U.S. National Library of Medicine, 2019. <http://www.clinicaltrials.gov> (accessed September 19, 2019).
- (25) Harris, L. J.; Larson, S. B.; Hasel, K. W.; McPherson, A. *Biochemistry* **1997**, *36* (7), 1581–97.
- (26) Tashiro, M.; Tejero, R.; Zimmerman, D. E.; Celda, B.; Nilsson, B.; Montelione, G. T. *J. Mol. Biol.* **1997**, *272* (4), 573–90.
- (27) *Jmol*, 2019. <http://www.jmol.org/> (accessed April 10, 2019).
- (28) Paszko, E.; Vaz, G. M.; Ehrhardt, C.; Senge, M. O. *Eur. J. Pharm. Sci.* **2013**, *48* (1), 202–210.
- (29) Bergstrom, L. C.; Vucenik, I.; Hagen, I. K.; Chernomorsky, S. A.; Poretz, R. D. *J. Photochem. Photobiol., B* **1994**, *24* (1), 17–23.
- (30) Yemul, S.; Berger, C.; Estabrook, A.; Suarez, S.; Edelson, R.; Bayley, H. *Proc. Natl. Acad. Sci. U. S. A.* **1987**, *84* (1), 246–50.
- (31) García-Díaz, M.; Nonell, S.; Villanueva, A.; Stockert, J. C.; Cañete, M.; Casadó, A.; Mora, M.; Sagristá, M. L. *Biochim. Biophys. Acta, Biomembr.* **2011**, *1808* (4), 1063–1071.
- (32) Broekgaarden, M.; van Vught, R.; Oliveira, S.; Roovers, R. C.; van Bergen en Henegouwen, P. M.; Pieters, R. J.; Van Gulik, T. M.; Breukink, E.; Heger, M. *Nanoscale* **2016**, *8* (12), 6490–4.
- (33) Morgan, J.; Gray, A.; Huehns, E. *Br. J. Cancer* **1989**, *59* (3), 366.
- (34) Morgan, J.; MacRobert, A.; Gray, A.; Huehns, E. *Br. J. Cancer* **1992**, *65* (1), 58.
- (35) Cui, S.; Yin, D.; Chen, Y.; Di, Y.; Chen, H.; Ma, Y.; Achilefu, S.; Gu, Y. *ACS Nano* **2013**, *7* (1), 676–88.
- (36) Derycke, A. S.; De Witte, P. A. *Int. J. Oncol.* **2002**, *20* (1), 181–7.
- (37) Barton, C. M.; Hall, P. A.; Hughes, C. M.; Gullick, W. J.; Lemoine, N. R. *J. Pathol.* **1991**, *163* (2), 111–6.
- (38) ClinicalTrials.gov Identifier: NCT03384238, Panitumumab-IRDye800 in Patients With Pancreatic Cancer Undergoing Surgery. *ClinicalTrials.gov*; U.S. National Library of Medicine, 2019 (accessed April 10, 2019).
- (39) Savellano, M. D.; Hasan, T. *Photochem. Photobiol.* **2003**, *77* (4), 431–439.
- (40) Bryden, F.; Maruani, A.; Rodrigues, J. M. M.; Cheng, M. H. Y.; Savoie, H.; Beeby, A.; Chudasama, V.; Boyle, R. W. *Bioconjugate Chem.* **2018**, *29* (1), 176–181.
- (41) He, C.; Liu, D.; Lin, W. *ACS Nano* **2015**, *9* (1), 991–1003.
- (42) He, C.; Duan, X.; Guo, N.; Chan, C.; Poon, C.; Weichselbaum, R. R.; Lin, W. *Nat. Commun.* **2016**, *7*, 12499.
- (43) Carter, K. A.; Luo, D.; Razi, A.; Geng, J.; Shao, S.; Ortega, J.; Lovell, J. F. *Theranostics* **2016**, *6* (13), 2329–2336.
- (44) Kamoun, W. S.; Oyama, S.; Kornaga, T.; Feng, T.; Luus, L.; Pham, M. T.; Kirpotin, D. B.; Marks, J. D.; Geddie, M.; Xu, L. *Nanoliposomal targeting of Ephrin receptor A2 (EphA2): Clinical translation*; AACR, 2016.
- (45) Dai, Q.; Wilhelm, S.; Ding, D.; Syed, A. M.; Sindhvani, S.; Zhang, Y.; Chen, Y. Y.; MacMillan, P.; Chan, W. C. W. *ACS Nano* **2018**, *12* (8), 8423–8435.
- (46) Mir, Y.; Elrington, S. A.; Hasan, T. *Nanomedicine* **2013**, *9* (7), 1114–22.
- (47) Ben-Dror, S.; Bronshtein, I.; Wiehe, A.; Röder, B.; Senge, M. O.; Ehrenberg, B. *Photochem. Photobiol.* **2006**, *82* (3), 695–701.
- (48) Obaid, G.; Jin, W.; Bano, S.; Kessel, D.; Hasan, T. *Photochem. Photobiol.* **2019**, *95* (1), 364–377.
- (49) Komatsu, T.; Moritake, M.; Nakagawa, A.; Tsuchida, E. *Chem. - Eur. J.* **2002**, *8* (23), 5469–80.
- (50) Lovell, J. F.; Jin, C. S.; Huynh, E.; Jin, H.; Kim, C.; Rubinstein, J. L.; Chan, W. C.; Cao, W.; Wang, L. V.; Zheng, G. *Nat. Mater.* **2011**, *10* (4), 324.
- (51) Rizvi, I.; Obaid, G.; Bano, S.; Hasan, T.; Kessel, D. *Lasers Surg. Med.* **2018**, *50* (5), 499–505.

- (52) Riske, K. A.; Sudbrack, T. P.; Archilha, N. L.; Uchoa, A. F.; Schroder, A. P.; Marques, C. M.; Baptista, M. S.; Itri, R. *Biophys. J.* **2009**, *97* (5), 1362–70.
- (53) Nathan, E.; Vijayashree, K.; Harikrishna, A.; Takafuji, M.; Jintoku, H.; Ihara, H.; Rao, N. M. *Photochem. Photobiol. Sci.* **2016**, *15* (12), 1476–1483.
- (54) Park, H.; Lee, J.; Jeong, S.; Im, B. N.; Kim, M. K.; Yang, S. G.; Na, K. *Adv. Healthcare Mater.* **2016**, *5* (24), 3139–3147.
- (55) Achalkumar, A. S.; Bushby, R. J.; Evans, S. D. *Soft Matter* **2010**, *6* (24), 6036–6051.
- (56) Zelphati, O.; Uyechi, L. S.; Barron, L. G.; Szoka, F. C., Jr. *Biochim. Biophys. Acta, Lipids Lipid Metab.* **1998**, *1390* (2), 119–33.
- (57) Cullis, P. R.; Chonn, A.; Semple, S. C. *Adv. Drug Delivery Rev.* **1998**, *32* (1–2), 3–17.
- (58) Richards, D. A.; Maruani, A.; Chudasama, V. *Chemical Science* **2017**, *8* (1), 63–77.
- (59) Kirchof, S.; Strasser, A.; Wittmann, H.-J.; Messmann, V.; Hammer, N.; Goepferich, A. M.; Brandl, F. P. *J. Mater. Chem. B* **2015**, *3* (3), 449–457.
- (60) Staros, J. V.; Wright, R. W.; Swingle, D. M. *Anal. Biochem.* **1986**, *156* (1), 220–2.
- (61) Oude Blenke, E.; Klaasse, G.; Merten, H.; Pluckthun, A.; Mastrobattista, E.; Martin, N. I. *J. Controlled Release* **2015**, *202*, 14–20.
- (62) Koo, H.; Lee, S.; Na, J. H.; Kim, S. H.; Hahn, S. K.; Choi, K.; Kwon, I. C.; Jeong, S. Y.; Kim, K. *Angew. Chem., Int. Ed.* **2012**, *51* (47), 11836–11840.
- (63) Baskin, J. M.; Prescher, J. A.; Laughlin, S. T.; Agard, N. J.; Chang, P. V.; Miller, I. A.; Lo, A.; Codelli, J. A.; Bertozzi, C. R. *Proc. Natl. Acad. Sci. U. S. A.* **2007**, *104* (43), 16793–7.
- (64) Elias, D. R.; Cheng, Z.; Tsourkas, A. *Small* **2010**, *6* (21), 2460–8.
- (65) Alam, S.; Alves, D. S.; Whitehead, S. A.; Bayer, A. M.; McNitt, C. D.; Popik, V. V.; Barrera, F. N.; Best, M. D. *Bioconjugate Chem.* **2015**, *26* (6), 1021–31.
- (66) Zhang, H.; Weingart, J.; Jiang, R.; Peng, J.; Wu, Q.; Sun, X.-L. *Bioconjugate Chem.* **2013**, *24* (4), 550–559.
- (67) Hui, J. Z.; Tsourkas, A. *Bioconjugate Chem.* **2014**, *25* (9), 1709–19.
- (68) Hui, J. Z.; Tamsen, S.; Song, Y.; Tsourkas, A. *Bioconjugate Chem.* **2015**, *26* (8), 1456–60.
- (69) Cheng, W. W.; Allen, T. M. *J. Controlled Release* **2008**, *126* (1), 50–8.
- (70) Cheng, W.; Allen, T. *Expert Opin. Drug Delivery* **2010**, *7* (4), 461–478.
- (71) Park, J. W.; Hong, K.; Kirpotin, D. B.; Colbern, G.; Shalaby, R.; Baselga, J.; Shao, Y.; Nielsen, U. B.; Marks, J. D.; Moore, D.; Papahadjopoulos, D.; Benz, C. C. *Clin. Cancer Res.* **2002**, *8* (4), 1172–81.
- (72) Iden, D. L.; Allen, T. M. *Biochim. Biophys. Acta, Biomembr.* **2001**, *1513* (2), 207–16.
- (73) Benveniste, M.; Livneh, E.; Schlessinger, J.; Kam, Z. *J. Cell Biol.* **1988**, *106* (6), 1903–9.
- (74) Savellano, M. D.; Hasan, T. *Clin. Cancer Res.* **2005**, *11* (4), 1658–68.
- (75) Beerli, R. R.; Graus-Porta, D.; Woods-Cook, K.; Chen, X.; Yarden, Y.; Hynes, N. E. *Mol. Cell. Biol.* **1995**, *15* (12), 6496–6505.
- (76) Abu-Yousif, A. O.; Moor, A. C.; Zheng, X.; Savellano, M. D.; Yu, W.; Selbo, P. K.; Hasan, T. *Cancer Lett.* **2012**, *321* (2), 120–127.
- (77) Heitner, T.; Moor, A.; Garrison, J. L.; Marks, C.; Hasan, T.; Marks, J. D. *J. Immunol. Methods* **2001**, *248* (1–2), 17–30.
- (78) Wileman, T.; Harding, C.; Stahl, P. *Biochem. J.* **1985**, *232* (1), 1–14.
- (79) Ritchie, M.; Tchistiakova, L.; Scott, N. *MAbs* **2013**, *5* (1), 13–21.
- (80) Rejman, J.; Oberle, V.; Zuhorn, I. S.; Hoekstra, D. *Biochem. J.* **2004**, *377* (1), 159–69.
- (81) Bareford, L. M.; Swaan, P. W. *Adv. Drug Delivery Rev.* **2007**, *59* (8), 748–58.
- (82) Takechi-Haraya, Y.; Goda, Y.; Sakai-Kato, K. *Mol. Pharmaceutics* **2017**, *14*, 2158.
- (83) Ma, H. L.; Jiang, Q.; Han, S.; Wu, Y.; Cui Tomshine, J.; Wang, D.; Gan, Y.; Zou, G.; Liang, X. *J. Mol. Imaging* **2012**, *11* (6), 487–98.
- (84) Zaroni, M.; Piccinini, F.; Arienti, C.; Zamagni, A.; Santi, S.; Polico, R.; Bevilacqua, A.; Tesei, A. *Sci. Rep.* **2016**, *6*, 19103.
- (85) Rahmzadeh, R.; Rai, P.; Celli, J. P.; Rizvi, I.; Baron-Lühr, B.; Gerdes, J.; Hasan, T. *Cancer Res.* **2010**, *70* (22), 9234–9242.
- (86) Bulin, A. L.; Broekgaarden, M.; Hasan, T. *Sci. Rep.* **2017**, *7* (1), 16645.
- (87) Rizvi, I.; Anbil, S.; Alagic, N.; Celli, J.; Zheng, L. Z.; Palanisami, A.; Glidden, M. D.; Pogue, B. W.; Hasan, T. *Photochem. Photobiol.* **2013**, *89* (4), 942–52.
- (88) Celli, J. P.; Rizvi, I.; Blanden, A. R.; Massodi, I.; Glidden, M. D.; Pogue, B. W.; Hasan, T. *Sci. Rep.* **2015**, *4*, 3751.
- (89) Waghray, M.; Yalamanchili, M.; Dziubinski, M.; Zeinali, M.; Erkkinen, M.; Yang, H.; Schradle, K. A.; Urs, S.; Pasca Di Magliano, M.; Welling, T. H.; Palmbos, P. L.; Abel, E. V.; Sahai, V.; Nagrath, S.; Wang, L.; Simeone, D. M. *Cancer Discovery* **2016**, *6* (8), 886–99.
- (90) Epstein Shochet, G.; Brook, E.; Eyal, O.; Edelstein, E.; Shitrit, D. *Am. J. Physiol.: Lung Cell. Mol. Physiol.* **2019**, *316*, L1025.
- (91) LeBleu, V. S.; Kalluri, R. *Dis. Models & Mech.* **2018**, *11* (4), No. dmm029447.
- (92) Smith, J. J.; Derynck, R.; Korc, M. *Proc. Natl. Acad. Sci. U. S. A.* **1987**, *84* (21), 7567–7570.
- (93) ClinicalTrials.gov Identifier: NCT03769506, Photoimmunotherapy (PIT) Study in Recurrent Head/Neck Cancer for Patients Who Have Failed at Least Two Lines of Therapy. *ClinicalTrials.gov*; U.S. National Library of Medicine, **2019** (accessed April 10, 2019).
- (94) DeLaney, T. F.; Sindelar, W. F.; Tochner, Z.; Smith, P. D.; Friauf, W. S.; Thomas, G.; Dachowski, L.; Cole, J. W.; Steinberg, S. M.; Glatstein, E. *Int. J. Radiat. Oncol., Biol., Phys.* **1993**, *25* (3), 445–57.
- (95) Mallidi, S.; Watanabe, K.; Timerman, D.; Schoenfeld, D.; Hasan, T. *Theranostics* **2015**, *5* (3), 289–301.
- (96) Boone, B. A.; Steve, J.; Krasinskas, A. M.; Zureikat, A. H.; Lembersky, B. C.; Gibson, M. K.; Stoller, R. G.; Zeh, H. J.; Bahary, N. J. *Surg. Oncol.* **2013**, *108* (4), 236–241.
- (97) Soukos, N. S.; Hamblin, M. R.; Hasan, T. *Photochem. Photobiol.* **1997**, *65* (4), 723–9.
- (98) Hamblin, M. R.; Miller, J. L.; Hasan, T. *Cancer Res.* **1996**, *56* (22), 5205–5210.
- (99) Molpus, K. L.; Hamblin, M. R.; Rizvi, I.; Hasan, T. *Gynecol. Oncol.* **2000**, *76* (3), 397–404.
- (100) Huang, H. C.; Pigula, M.; Fang, Y.; Hasan, T. *Small* **2018**, *14*, No. e1800236.
- (101) Kullmann, F.; Hartmann, A.; Stohr, R.; Messmann, H.; Dollinger, M. M.; Trojan, J.; Fuchs, M.; Hollerbach, S.; Harder, J.; Troppmann, M.; Kutscheid, A.; Endlicher, E. *Oncology* **2011**, *81* (1), 3–8.
- (102) del Carmen, M. G.; Rizvi, I.; Chang, Y.; Moor, A. C.; Oliva, E.; Sherwood, M.; Pogue, B.; Hasan, T. *J. Natl. Cancer Inst.* **2005**, *97* (20), 1516–24.

Supporting Information

Impacting Pancreatic Cancer Therapy in Heterotypic *In Vitro* Organoids and *In Vivo* Tumors with Specificity-Tuned, NIR-Activable Photoimmunonanoconjugates: Towards Conquering Desmoplasia?

Girgis Obaid,^[a] Shazia Bano,^[a] Srivalleesha Mallidi,^{[a],[b]} Mans Broekgaarden,^[a] Jerrin Kuriakose,^[a] Zachary Silber,^[a] Anne-Laure Bulin,^[a] Yucheng Wang,^[a] Zhiming Mai,^[a] Wendong Jin,^[a] Diane Simeone^[c] and Tayyaba Hasan^{[a][d]}*

[a] Wellman Center for Photomedicine, Massachusetts General Hospital and Harvard Medical School, Boston, Massachusetts 02114, United States

[b] Current affiliation: Department of Biomedical Engineering, Tufts University, Medford, Massachusetts, 02155, United States

[c] Department of Surgery and Department of Pathology, Perlmutter Cancer Center, New York University Langone Health, New York City, New York 10016, United States

[d] Division of Health Sciences and Technology, Harvard University and Massachusetts
Institute of Technology, Cambridge, Massachusetts 02139, United States

KEYWORDS: nanoengineering, photoimmunonanoconjugates, pancreatic ductal adenocarcinoma, NIR photodynamic activation, heterotypic organoids

MATERIALS AND METHODS

Site-specific Protein Z-N₃ conjugation to Cetuximab: An azido moiety was site-specifically introduced to the Fc region of cetuximab (Cet) through a photocross-linked recombinant Protein Z (Pz) intermediate, tethered to a terminal azido fluorescent peptide. The Pz-FP-N₃ construct, referred to as **Pz-N₃** from hereon, was covalently tethered to the Fc region of Cet by the photocross-linking of benzoylphenylalanine (BPA), engineered into the IgG binding domain of the recombinant Pz. The expression, isolation and site-specific photocross-linking of Pz-N₃ to Cet was as described below.

a) expression of Pz: Pz containing the unnatural amino acid photocross-linker, BPA, at the IgG binding site was expressed as previously reported.^[1] Briefly, T7 Expression Crystal Competent Cells (New England Biolabs, Ipswich, MA) co-transformed with a pEVOL-pBpF plasmid (Addgene, Cambridge, MA) encoding the BPA incorporation machinery and the pSrtA-Pz plasmid (Integrated DNA Technologies, Coralville, IA) encoding the Sortase-Pz construct were cultured overnight at 37°C on agar plates containing ampicillin (250 µg/ml; Thermo Fisher Scientific) and chloramphenicol (100 µg/ml; Thermo Fisher Scientific). The cells were a kind gift from Dr. Andrew Tsourkas, University of Pennsylvania. Cloning of the Pz fusion protein vector was performed as previously described.^[2] Ampicillin and chloramphenicol select for cells expressing both Pz and pEVOL-BPA, respectively. Ampicillin (100 µg/ml final concentration) and chloramphenicol (25 µg/ml final concentration) were added to Overnight Express Autoinduction

media (AI media, 100 ml; EMD Milipore). Arabinose (10% stock in water; Thermo Fisher Scientific) was added to the AI media at a 1:100 dilution to induce pEVOL-BPAX. 4-benzoyl-L-phenylalanine (BPA, 10 mM stock in 100 mM NaOH; Alfa Aesar) was added to the AI media at a 1:300 dilution). A single colony from the co-transformed T7 Expression Crystal Competent Cells cultured on the agar plates was inoculated into the AI media prepared. The cells were grown at 37°C and monitored at 600 nm to obtain an OD of 0.4-0.6. Isopropyl β -D-1-thiogalactopyranoside (IPTG, 500 mM stock in water; Thermo Fisher Scientific) was added to the cells cultured in AI media at a 1:1000 dilution to induce protein expression. The cells were allowed to express for 48 h at 37°C. The cells were centrifuged at 5,500 \times g for 7 min, the supernatant was aspirated, and the cell pellets were lysed with Bacterial Protein Extraction Reagent (B-PER; Pierce) containing EDTA-free protease inhibitor tablets (Roche) at a ratio of 1 g cell pellet to 4 ml B-PER reagent. The cells were incubated for 20 min at room temperature in the B-PER reagent, then sonicated for 15 cycles of 5s pulses using a Fisher Sonic Dismembrator Model 300 sonicator operating at 40%. Following each pulse, the cell lysates were cooled on ice to prevent overheating. The lysate was centrifuged at 10,000 \times g at 4°C for 10 min in microcentrifuge tubes to pellet insoluble cell debris.

b) Isolation of Pz-azido fluorescent peptide (Pz-N₃): TALON Metal Affinity slurry (2 ml; Clontech) was packed into 10 ml poly-prep columns (Bio-Rad Laboratories, Inc.), washed once with 8 ml Milli-Q water and twice with 8 ml 1x DPBS (no calcium or magnesium, Corning). The stopper was attached to the column, the pooled clarified bacterial supernatant was loaded onto the column and the column were capped. The column was then orbitally rotated at room temperature for 30 min in the dark to allow the expressed His-tag fusion protein to bind to the resin. The flow-through was then drained from the column and the column was washed three times with 8 ml 1x DPBS. The column was then loaded with the heterobifunctional azido fluorescent peptide (FP-N₃)

sequence (NH₂-Gly-Gly-Gly-Lys(5-FAM)-Gly-Gly-Ser-Lys(N₃)-NH₂; 1 ml, 200 μM in 1x DPBS, 1030 g/mol; AnaSpec Inc.) containing calcium chloride dihydrate (50 μM, 147.01 g/mol; Sigma-Aldrich) and the stopper was attached to the column. The FP-N₃ sequence (NH₂-Gly-Gly-Gly-Lys(5-FAM)-Gly-Gly-Ser-Lys(N₃)-NH₂)^[1] contains a triglycine sequence to mediate sortase cleavage and conjugation to Pz, a fluorescent 5-FAM molecule for quantitation and a terminal azide to mediate click conjugation to the photoimmunonanoconjugates (PINs). The resin was mixed to evenly distribute the FP-N₃ and calcium chloride, and the column was incubated for 6 h at 37°C to allow for sortase cleavage and FP-N₃ ligation to Pz. The conjugate of Pz with FP-N₃ (Pz-N₃) cleaved off the resin by sortase was eluted from the column using 2 ml 1x DPBS and analyzed using denaturing SDS-PAGE. The Pz-N₃ was lyophilized and each 100 ml culture equivalent of lyophilized Pz-N₃ was reconstituted in 100 μl of Milli-Q water. The Pz-N₃ concentration was determined using the 5-FAM absorbance ($\epsilon_{492 \text{ nm}} = 82,000 \text{ M}^{-1} \cdot \text{cm}^{-1}$), which exists at a 1:1 ratio when the peptide is tethered to the Pz. The Pz-N₃ was then stored at 4°C in the dark until site-specific photocross-linking to Cet.

c) Site-specific photocross-linking of Pz-N₃ to Cet: Pz-N₃ was mixed with Cet (2 mg/ml in 1x DPBS, 145781.6 g/mol (FASTA sequence analysis), Erbitux ; Ely Lilly) at a 3:2 molar ratio for 1 h at room temperature in the dark to allow for the site-specific non-covalent binding of Pz-N₃ to the Fc region of Cet. The Cet-Pz-N₃ complex was placed in transparent 96 well multidishes in 100 μl aliquots and irradiated at 365 nm for 90 min on ice using a 115V Handheld LW 6W UV lamp (UVL-56; UVP). The UV-irradiated Cet-Pz-N₃ mixture was then buffer exchanged with glycine-HCl buffer (200 mM, pH 3.5) by centrifugation in a 30 kDa ultrafiltration tube (EMD Millipore) at 5,000 xg for 5 min at 4°C then incubated in the dark at room temperature for 10 min to allow the dissociation of non-covalently bound Pz-N₃. The Cet-Pz-N₃ mixture in glycine-HCl buffer was

then loaded onto a 10 mL borosilicate Poly-Prep chromatography column (Bio-Rad) packed with prep grade Superdex 75 (GE Healthcare Life Sciences), equilibrated with 1x DPBS using a syringe pump at a flow rate of 0.05 ml/min. The higher molecular weight fraction consisting of the photocross-linked Cet-Pz-N₃ was collected and concentrated by centrifuging in 30 kDa ultrafiltration tubes (EMD Milipore) at 2,500 xg for 20 min at 4°C. UV-Visible spectrophotometry was used to determine the concentrations of Cet ($\epsilon_{280\text{ nm}} = 217,315\text{ M}^{-1}\cdot\text{cm}^{-1}$ (Expasy ProtParam Tools))^[31] and of 5-FAM, which corresponds to the Pz-N₃ photocross-linked to the Cet ($\epsilon_{492\text{ nm}} = 82,000\text{ M}^{-1}\cdot\text{cm}^{-1}$). The purified Cet-Pz-N₃ was stored in the dark at 4°C until needed for click conjugation to the PINs.

Stochastic NHS-PEG₄-N₃ conjugation to Cet: In an alternative strategy, an azido moiety was stochastically introduced to Cet through the conjugation of *N*-hydroxysuccinimidyl azido poly(ethylene glycol)₄ (NHS-PEG₄-N₃, 388.37 g/mol; Thermo Fisher Scientific) to the antibody's lysine residues. The NHS ester of Alexa Fluor 488 (AF488-NHS, 643.4 g/mol; Thermo Fisher Scientific) was also conjugated to Cet to assist in quantitation following PIN fabrication. Stock solutions of NHS-PEG₄-N₃ (10 mg/ml) and AF488-NHS (1 mg/ml) in anhydrous dimethyl sulfoxide (DMSO; Sigma-Aldrich) were mixed at quantities corresponding to a 2.5-fold molar excess of each molecule to Cet prior to addition of the antibody. Cet (2 mg/ml in 1x DPBS) was then added to the NHS-PEG₄-N₃ and AF488-NHS mixture and was further mixed by orbital rotation for 24 h at 4°C. Unreacted NHS-PEG₄-N₃ and AF488-NHS were removed from the conjugated Cet by size exclusion chromatography using illustra NAP Columns (GE Healthcare Life Sciences) equilibrated with 1x DPBS. The purified Cet conjugated to both AF488 and PEG₄-N₃ (Cet-PEG₄-N₃) was collected and concentrated by centrifuging in 30 kDa ultrafiltration tubes (EMD Milipore) at 2,500 xg for 20 min at 4°C. UV-Visible spectrophotometry was used to

determine the concentrations of Cet as described earlier and AF488 ($\epsilon_{494 \text{ nm}} = 71,000 \text{ M}^{-1} \cdot \text{cm}^{-1}$ (Invitrogen Manual MAN0002151)). The purified Cet-PEG₄-N₃ was stored in the dark at 4°C until needed for click conjugation to the nanoconstructs. It was determined that 1.07 PEG₄ azide molecules were conjugated to each Cet molecule, as validated using a 10x reaction with Cy5-DBCO ($\epsilon_{650 \text{ nm}} = 250,000 \text{ M}^{-1} \cdot \text{cm}^{-1}$) and subsequent purification with Sephadex G25 (superfine) size exclusion chromatography.

Denaturing gel electrophoresis of Cet-Pz and Cet-PEG₄-N₃: Free Cet, Cet-Pz and Cet-PEG₄-N₃ in PBS were denatured with mercaptoethanol, loaded onto Mini-PROTEAN TGX (Bio-Rad) 4-20% acrylamide gels and then ran for 1 h with Precision Plus Protein Dual Xtra Standards (Bio-Rad). The gels were removed from the cassettes and soaked in GelCode Blue Safe Protein Stain (Thermo Fisher Scientific) for 20 min in the dark. The gels were then de-stained in multiple Milli-Q water washes and imaged using a Gel Logic 200 Imaging System (Kodak).

Synthesis of the BPD conjugates of 16:0 lyso PC and 20:0 lyso PC: The carboxylate of the benzoporphyrin derivative photosensitizer was coupled to the hydroxyl moiety of the phospholipid 1-palmitoyl-2-hydroxy-sn-glycero-3-phosphocholine (16:0 lyso PC) using Steglich esterification, according to an adaptation of a previously reported protocol for porphyrins^[4] and directly as reported previously by our group.^[5] Briefly, the following constituents were mixed at a 1 : 5 : 50 : 25 : 300 molar ratio, respectively: 16:0 lyso PC (495.63 g/mol, chloroform; Avanti Polar Lipids, Inc.), benzoporphyrin derivative monoacid ring A (BPD, verteporfin, mixed isomers, 718.79 g/mol; U.S. Pharmacopeia (USP)), 1-ethyl-3-(3dimethylaminopropyl) carbodiimide (EDC, 155.24 g/mol; Sigma-Aldrich), 4-(dimethylamino)pyridine (DMAP, 122.17 g/mol; Sigma-Aldrich), and *N,N*-Diisopropylethylamine (DIPEA, 129.24 g/mol. 0.742 g/ml; Sigma-Aldrich). The mixture was dissolved in dichloromethane (DCM, 5 ml, ACS Reagent Grade, 99.5%; Sigma-Aldrich) and

rigorously stirred at 2500 RPM for 72 h at room temperature in the dark using a magnetic stir plate. The 16:0 lyso PC-BPD lipid conjugate (16:0 BPD-PC) was purified using Analtech Preparative Thin Layer Chromatography Silica Uniplates (Sigma-Aldrich) running on a mobile phase consisting of 10% methanol in DCM. The 16:0 BPD-PC-containing silica fraction ($R_f = 0.144$) was removed from the TLC plate and the conjugate was extracted by sonication in 33% methanol in DCM for 10 min. The silica was sedimented by centrifugation at 3,700 $\times g$ for 10 min and the supernatant containing the extracted 16:0 BPD-PC was collected into a round-bottom flask. The silica fraction was washed two further times and all 16:0 BPD-PC solutions were pooled into the round bottom flask. The solvent mixtures were removed from the extract by rotary evaporation under reduced pressure at 40°C connected to a liquid nitrogen trap condenser. Residual silica previously solubilized in the 33% methanol in DCM solvent mixture was removed by redissolving the dried 16:0 BPD-PC extract in pure DCM. The insoluble silica precipitate was removed by filtration using a Fisherbrand poly(tetrafluoroethylene) (PTFE) filter (0.22 μm pore size, 13 mm diameter; Thermo Fisher Scientific) driven by a gastight glass syringe. The DCM was removed from the filtered 16:0 BPD-PC solution using rotary evaporation as described and the purified conjugate was redissolved in chloroform and stored in the dark at -20°C. The concentration of the 16:0 BPD-PC was determined by diluting the phospholipid conjugate in DMSO and measuring the UV-Visible absorption spectrum using $\epsilon_{687\text{ nm}} = 34,895\text{ M}^{-1}\cdot\text{cm}^{-1}$. The lysophospholipid 1-arachidoyl-2-hydroxy-*sn*-glycero-3-phosphocholine (20:0 lyso PC) was conjugated to BPD using the same procedure. The lipid conjugates were validated with MALDI using 3,4-dihydroxybenzoic acid (10mg/ml in ethanol; Sigma Aldrich) as a matrix. The expected M.W. of 16:0 BPD-PC (99.02% purity by HPLC) is 1196.41 g/mol, the observed M.W. is 1197.123 m/z. The expected M.W. of 20:0 BPD-PC (95.52% purity by HPLC) is 1252.52 g/mol, the observed M.W. is

1255.715 m/z. Purity was assessed using HPLC with a gradient of 95/5 water/acetonitrile (0.1% TFA) to 5/95 water/acetonitrile (0.1% TFA) over 30 minutes, followed by a 30 minute hold at 5/95 water/acetonitrile (0.1% TFA).

Synthesis of the BPD conjugate of DSPE-PEG₂₀₀₀-NH₂: BPD was conjugated to DSPE-PEG₂₀₀₀-NH₂ using EDC amide coupling as we have described previously.^[51] Briefly, DSPE-PEG₂₀₀₀-NH₂ in chloroform was mixed with a 10-fold molar excess of BPD and a 5-fold molar excess of EDC to BPD in a 13 x 100 mm Pyrex tube. The mixture was stirred in the dark at 2500 RPM for 72 h. The chloroform was then evaporated using a flow of nitrogen and the dry reaction mixture was dissolved in 1ml methanol. The reaction mixture was then run through Sephadex LH-20 (GE Healthcare Life Sciences) equilibrated with methanol, and the fastest running colored fraction consisting of DSPE-PEG₂₀₀₀-BPD was collected. The methanol was evaporated, and the DSPE-PEG₂₀₀₀-BPD was dissolved in chloroform and stored in the dark at -20°C. The concentration of the DSPE-PEG₂₀₀₀-BPD was determined by diluting the conjugate in DMSO and measuring the UV-Visible absorption spectrum using $\epsilon_{687 \text{ nm}} = 34,895 \text{ M}^{-1} \cdot \text{cm}^{-1}$. The DSPE-PEG₂₀₀₀-BPD conjugate (97.27% purity by HPLC) was validated with MALDI as described earlier. The expected M.W. is 3479.25 g/mol and the observed M.W. is 3588.481 m/z. This discrepancy is due to the normal distribution of all PEG chain lengths conjugated to DSPE.

Nanoconstruct synthesis: All liposomal nanoformulations were prepared using the hydrated lipid film process. Lipid films were prepared in 13 x 100 mm Pyrex tubes using chloroform solutions of 1,2-dipalmitoyl-sn-glycero-3-phosphocholine (DPPC, 734.04 g/mol), 1,2-dioleoyl-3-trimethylammonium-propane (chloride salt) (DOTAP, 698.54 g/mol) OR 1,2-dioleoyl-sn-glycero-3-phospho-(1'-rac-glycerol) (sodium salt) (DOPG, 797.026 g/mol), cholesterol (386.65 g/mol), 1,2-distearoyl-sn-glycero-3-phosphoethanolamine-N-[methoxy(polyethyleneglycol)-2000]

(ammonium salt) (DSPE-mPEG₂₀₀₀, 2805.50 g/mol) and 1,2-distearoyl-sn-glycero-3-phosphoethanolamine-N-[dibenzocyclooctyl(polyethylene glycol)-2000] (ammonium salt) (DSPE-PEG₂₀₀₀-DBCO, 3077.80 g/mol), all purchased from Avanti Polar Lipids, Inc. DPPC, DOTAP/DOPG, cholesterol, DSPE-mPEG₂₀₀₀ and DSPE-PEG₂₀₀₀-DBCO were mixed at a molar ratio of 0.582 : 0.079 : 0.289 : 0.045 : 0.005, respectively. PEGylated DSPE was consistently kept at a total of 5 mol %, with 0.5 mol% substituted for DSPE-PEG₂₀₀₀-DBCO to mediate the copper-free click conjugation to azide-derivatized Cet. The BPD or its lipidated variants (16:0 BPD-PC, 20:0 BPD-PC, cholesterol-BPD or DSPE-PEG₂₀₀₀-BPD), were introduced to the lipid mixture at 0.6 mol%, replacing their respective DPPC molar fraction. All lipids were briefly vortexed (Fisher Scientific Analog Vortex Mixer) and the chloroform was evaporated using a flow of nitrogen gas through a 16-gauge needle with continuous rotation to form the thin lipid film. Residual chloroform was removed by storing the lipid film under vacuum overnight. The dried lipid film was hydrated in 1x DPBS (1 ml; Corning) using 5 cycles of the freeze-thaw-vortex method by incubating in a darkened water bath at 42°C for 10 min, vortexed for 30 s, then incubated in ice for 10 min. To prepare monodisperse unilamellar liposomal nanoconstructs, the lipid suspensions were extruded 11 times at 42°C through two polycarbonate membranes, (0.1 µm pore size, 19 mm diameter; Avanti Polar Lipids, Inc.) using an Avanti Mini-Extruder kit. The nanoconstructs were stored at 4°C in the dark. The concentration of the BPD variants within the nanoconstruct formulations was determined using UV-Visible absorption spectroscopy ($\epsilon_{687\text{ nm}} = 34,895\text{ M}^{-1}\cdot\text{cm}^{-1}$) in DMSO dilutions. The majority of the nanoconstructs were prepared using 16:0 BPD-PC, which will be referred to as BPD-PC from hereon for simplicity. The experiments measuring the photobleaching of BPD nanoconstructs and BPD-PC nanoconstructs were performed in 1xPBS in

black-walled, transparent base 96 well plates (Thermo Fisher Scientific) irradiated with 690 nm light at an irradiance of 150 mW/cm².

Site-specific (Cet-Pz-N₃) and stochastic (Cet-PEG₄-N₃) conjugation to nanoconstructs using copper-free click chemistry: Both Cet-Pz-N₃ and Cet-PEG₄-N₃ in 1x DPBS were reacted with the BPD-PC nanoconstructs at lipid : Cet mass ratios of 1:0.02, 1:0.05, 1:0.1, 1:0.15 or 1:0.2 and incubated at room temperature for 24 h with continuous orbital rotation. Following copper-free click conjugation of surface DSPE-PEG₂₀₀₀-DBCO to the azide moieties on site-specifically (Cet-Pz-N₃) or stochastically (Cet-PEG₄-N₃) conjugated Cet, unbound antibody was removed from the PINs using 10 mL borosilicate Poly-Prep chromatography columns (Bio-Rad) packed with Sepharose CL-4B (Sigma-Aldrich), equilibrated with 1x DPBS using a syringe pump at a flow rate of 0.05 ml/min. The eluted colored fractions consisting of Cet-Pz-N₃ PINs and Cet-PEG₄-N₃ PINs were collected and stored in the dark at 4°C. The molar concentration of nanoconstructs was calculated using the molar concentration of lipid within a typical formulation (34.043 mM) and the approximation that a unilaminar nanovesicle with a hydrodynamic diameter of 100 nm is formed of 80,000 lipids, based on the following equation.^[6]

$$N_{tot} = \frac{\left[4\pi \left(\frac{d}{2}\right)^2 + 4\pi \left(\frac{d}{2} - h\right)^2 \right]}{a}$$

N_{tot} is the total number of lipids per nanovesicle, d is the hydrodynamic diameter in nanometers and h is the thickness of the bilayer in nanometers, which approximates to 5 nm. For a phosphatidylcholine nanoconstruct preparation such as the one used in this study, this equation can be simplified further to the following equation.

$$N_{tot} = 17.69 \times \left[\left(\frac{d}{2}\right)^2 + \left(\frac{d}{2} - 5\right)^2 \right]$$

Once the total number of lipids per nanoconstruct was obtained, the molar concentration of nanoconstructs was derived and used for approximating the quantities of Cet-Pz-N₃ and Cet-PEG₄-N₃ conjugated. The concentration of the BPD-PC within the PIN formulations was determined using UV-Visible absorption spectroscopy ($\epsilon_{687\text{ nm}} = 34,895\text{ M}^{-1}\cdot\text{cm}^{-1}$) in DMSO dilutions. The degree of conjugation of Cet-Pz-N₃ and Cet-PEG₄-N₃ to the PINs was determined using fluorimetry with standard curves of free Cet variants in 1x DPBS, generated using Exc_{480 nm}/Emi_{521 nm} (for 5-FAM on the Cet-Pz-N₃) or Exc_{480 nm}/Emi_{517 nm} (for AF488 on the Cet-PEG₄-N₃) and an integration time of 0.1 s. Fluorescence emission values of 1xDPBS dilutions (100-200-fold) of each purified Cet-Pz-N₃ and Cet-PEG₄-N₃ PINs, were normalized to the BPD-PC concentration within each preparation. The autofluorescence of BPD-PC nanoconstructs not conjugated to antibodies was obtained under the same excitation parameters and then normalized to the BPD-PC concentrations. This normalized autofluorescence was subtracted from the normalized fluorescence of Cet-Pz-N₃ and Cet-PEG₄-N₃ PINs. The Cet-Pz-N₃ and Cet-PEG₄-N₃ standard curves were used to derive the molar concentrations of the Cet click-conjugated to the PINs. The normalized molar concentrations of the click-conjugated Cet-Pz-N₃ and Cet-PEG₄-N₃ were used to derive the absolute number of antibodies conjugated to each nanoconstruct and the respective degree of conjugation.

Chemotherapy-loaded Cet-PINs: Cet-PINs conjugated to Cet-PEG₄-N₃ molecules were fabricated as described above, with slight modifications in the fabrication process. The lipid films were doped with 100 nmoles of 16:0 BPD-PC and were hydrated in 1ml of either gemcitabine hydrochloride (15 mg/ml; LC Labs), Oxaliplatin (7.5 mg/ml; SelleckChem) or 5-fluorouracil (10 mg/ml; Sigma-Aldrich). Following extrusion using 200 nm polycarbonate membranes, all liposomes were purified from unencapsulated chemotherapy using Sepharose CL-4B columns equilibrated with PBS. Purified liposomes were conjugated to Cet-PEG₄-N₃ as described above

and purified once more after 24 h conjugation. Encapsulated chemotherapy was quantified using Agilent 6430 Triple Quad LC-MS/MS (oxaliplatin: 397 m/z precursor, 344 m/z product ion, 75 fragmentor, 15 collision energy, 7 accelerator voltage, positive ion mode; gemcitabine hydrochloride: 264 m/z precursor, 112 m/z product ion, 75 fragmentor, 15 collision energy, 7 accelerator voltage, positive ion mode; 5-fluorouracil: 129 m/z precursor, 42 m/z product ion, 90 fragmentor, 20 collision energy, 7 accelerator voltage, negative ion mode.)

Cell Culture: All cells were cultured in Corning T75 cell culture flasks (Corning). DMEM media supplemented with 1x Penicillin/Streptomycin and 10% heat-inactivated fetal bovine serum (FBS, Gibco) was used to culture A431 cells (ATCC) and MIA PaCa-2 cells (ATCC). RPMI media with glutamine supplemented with 1x Penicillin/Streptomycin and 10% heat-inactivated FBS was used to culture OVCAR-5 cells (NIH) and T47D cells (ATCC). CHO-WT and CHO-EGFR cells were kindly provided by Dr. T. Heitner at the Department of Anesthesiology, UCSF, San Francisco, California,^[7] and were cultured in Ham's F12k media supplemented with 1x Penicillin/Streptomycin and 10% heat-inactivated FBS. CHO-EGFR cells were selected prior to use by supplementing the media with G-418 (0.8 mg/ml; Sigma Aldrich), which was removed two passages before molecular targeted NIR photodynamic activation of the cells. Cells were passaged by trypsinization using 0.05% Trypsin (Corning).

Flow Cytometry Analyses: Confluent cells grown in monolayer in Corning T75 cell culture flasks (Corning) were washed once with 5 ml of 1x DPBS (without calcium or magnesium, Corning) and once with 2 ml of 0.05% Trypsin (Corning). The cells were then incubated at 37°C for a maximum of 3 min with mild agitation every 1 min. The detached cell suspensions were collected in media containing 10% FBS and centrifuged for 5 min at 1,000 xg, the supernatant was aspirated and discarded, and the cells were redispersed in their respective culture media containing 10%

FBS. Following 40 repeated 10 ml pipette agitations to prepare single-cell suspensions, the cells were counted using a Coulter counter and 50,000 cells were placed into 1.5 ml microcentrifuge tubes. The cells were pelleted by centrifugation for 5 min at 1,000 xg, the media in the supernatant was discarded and replaced with 100 μ l of the respective serum-containing culture media containing the PIN formulations (250 nM BPD equivalent). It must be noted that in the serum IgG concentration is 1.9mg/ml in the final PIN dilutions prepared in media containing 10% FBS.^[8] Following 10 repeated pipette agitations to prepare single-cell suspensions, the cells were incubated at 37°C for 15 min in the dark. The cells were then pelleted again by centrifugation for 5 min at 1,000 xg, the media containing the PIN formulations in the supernatant was discarded and replaced with 200 μ l 1x DPBS (without calcium or magnesium, Corning) and cooled to 4°C. Following 10 pipette agitations to prepare single-cell suspensions, the cells in 1x DPBS were transferred to flow cytometry tubes and temporarily stored on ice in the dark. For each condition, 10, 000 cells were analyzed using a BD FACSAria II flow cytometer (BD Biosciences). Fluorescence of cell-associated BPD-PC was measured using a 405 nm laser, a 610 nm dichroic long pass filter and a simultaneous 620 nm long pass filter. Fluorescence of the 5-FAM and the AF 488 were measured using a 405 nm laser and a 450/40 nm filter. When blocking with a Cet concentration that matches free IgG, 1 mg/ml of Cet was used and the final concentration of FBS was made to 5%, which equates to a final mean IgG concentration of 0.95 mg/ml that serves as an irrelevant antibody sham control throughout all in vitro experiments.^[8] A control for competitive inhibition was also performed using a human IgG isotype control (Pierce).

Physical characterization of PINs: Z-average diameters, polydispersity indices and ζ -potentials of PINs were measured using a Zetasizer Nano ZS (Malvern Instruments Ltd.). For simultaneous z-average diameter and polydispersity index measurements, 2 μ l of PINs were placed in a 4 ml

polystyrene 4xOptical cuvette (Sarstedt AG & Co.) and 1 ml of 1x DPBS was added to the PINs. Temperature equilibration (120 s) was completed prior to the three individual measurements performed for each sample. ζ potential measurements were performed using a Folded Zeta Capillary Cell (Malvern Instruments Ltd.). 10 μ l of PINs were diluted with 1 ml of 3 mM NaCl, loaded into the cell and three individual measurements were performed for each sample.

Cellular uptake studies: OVCAR-5 cells were trypsinized and seeded onto NUNC treated, black-walled, transparent base 96 well plates (Thermo Fisher Scientific) at a density of 50,000 cells per well for 24 h. PIN dilutions (250 nM BPD equivalent) prepared in RPMI media containing 10% FBS were added to the cells and incubated at 37°C. At the required time-points, the media containing PINs was aspirated from the wells and the cells were washed three times with 100 μ l 1x DPBS (without calcium or magnesium, Corning). Finally, the cells were digested in 50 μ l Solvable (PerkinElmer) tissue digestion solution, the BPD equivalent fluorescence was measured using a plate reader (SpectraMAX M5), and the BPD equivalent concentration was determined using standard curves prepared in Solvable. The protein concentration in each respective well was then measured using the Pierce BCA Protein Quantitation Kit (Thermo Fisher Scientific) and the BPD equivalent concentration was normalized to protein concentration for each well.

Confocal microscopy: OVCAR-5 cells were trypsinized and seeded onto glass bottom, black-walled 96 well plates (Thermo Fisher Scientific) at a density of 5,000 cells per well. PIN dilutions (250 nM BPD-PC equivalent) were prepared in RPMI media containing 10% FBS and were incubated for 6 h or 24 h at 37°C. Hoechst 33342 or LysoTracker Red DND-99 (Thermo Fisher Scientific) were added to the cells according to the manufacturer's protocols. The nuclei were visualized with the Hoechst stain (405 nm laser), the PINs were visualized using the BPD-PC fluorescence (405 nm laser) and the lysosomes were visualized using the LysoTracker (488 nm

laser). For visual clarity, all blue channel images were uniformly set to 1-100, red channel images were uniformly set to 6-40, and green channel images were uniformly set to 1-80. All quantitative image analyses of colocalization were performed using unmodified images. Colocalization analysis of the BPD-PC-containing PINs and the lysosome-specific LysoTracker marker was performed using confocal microscopy and a subsequent custom-developed MATLAB routine to analyze the images. The imaging was performed using a confocal microscope (Olympus FV1000) through a 60X objective (1.2NA, Water). For each field of view, a bright-field image and fluorescence images were acquired simultaneously. Image analysis initially highlighting each group of cells from the bright-field image. Then, the fluorescence images were binarized using a threshold defined by control images of untreated cells. Finally, for each object identified on the bright-field image, pixels exhibiting signals in both the BPD-PC channel and the LysoTracker channel were counted and converted into a metric termed 'colocalization area'. The ratio of photosensitizer colocalized with the LysoTracker was calculated by dividing this colocalization area by the total area occupied by the BPD-PC nanoconstructs.

Molecular targeted NIR photoactivation in 2D cells: At 60-80% confluence, A431 cells, OVCAR-5 cells, T47D cells and MIA PaCa-2 cells were seeded onto NUNC treated, black-walled, transparent base 96 well plates (Thermo Fisher Scientific) at a density of 1,500 cells per well 24 h before treatment. CHO-WT and CHO-EGFR cells were seeded onto the same 96 well plate type at a density of 400 cells/well 24 h prior to experimentation. PIN dilutions prepared in the respective FBS-containing cell culture media were prepared and incubated with cells for 6 h at 37°C. The PINs were then removed from the cells, replaced with fresh respective FBS-containing cell culture media and irradiated using an Intense 7401 690 nm laser with a fluence of 20 J/cm² at an irradiance of 150 mW/cm². Irradiance was measured using a Vega Handheld Power Meter (Ophir). Following

molecular targeted NIR photoactivation, the cells were incubated for 72 h prior to assessing the viability. The media was removed from the cells and replaced with fresh respective FBS-containing cell culture media containing 3-(4,5-Dimethylthiazol-2-yl)-2,5-Diphenyltetrazolium Bromide (MTT, 0.1 mg/ml; Sigma-Aldrich) and incubated for 1 h at 37°C (T47D cells were incubated for 1.5h). The media containing MTT was then removed from the cells, the formazan was dissolved in DMSO and the absorbance was measured at 517 nm. Viability was calculated as a percentage absorbance at 517 nm with respect to untreated control cells.

Cet-PIN selectivity and penetration in monotypic and heterotypic PDAC organoids: Fluorescent Cet-PIN constructs were prepared as previously described without doping of 16:0 BPD-PC. The DSPE-PEG lipid content was modified to incorporate an amino terminal lipid for fluorophore conjugation as such; DSPE-mPEG₂₀₀₀ (4.3 mol%), DSPE-PEG₂₀₀₀-DBCO (0.5 mol%) and DSPE-PEG₂₀₀₀-NH₂ (0.2 mol%). Lipid films were prepared and hydrated in 1xDPBS as described earlier. The Alexa Fluor 680 NHS (AF680-NHS) ester was reacted with the PINs at a 5-fold molar excess to DSPE-PEG₂₀₀₀-NH₂ for 24 h at room temperature. Unreacted AF680 was removed by dialysis against 1x PBS in 100 kDa Float-A-Lyzer dialysis tubes (Spectrum Labs) at 4°C for 48 h. Cet-PEG₄-N₃ was reacted with the nanoconstructs as described earlier to prepare Cet-PINs, which were then purified using Sepharose CL-4B size exclusion chromatography equilibrated with 1x DPBS. Untargeted AF680 tagged nanoconstructs were prepared as a control. Lipid content was quantified by back calculation from the AF680 concentration that was determined using UV-visible spectrophotometry and an extinction coefficient $\epsilon_{694\text{ nm}} = 182,000\text{ M}^{-1}\cdot\text{cm}^{-1}$. The same procedure was used to generate Cet-PIN-IRDye800 constructs for photoacoustic imaging.

MIA PaCa-2 cells (2,500 cells per well) were cultured in DMEM with 10% FBS for 48 h in Corning Costar Ultra-Low attachment 96 well plates in the absence or presence of patient-derived

Pancreatic Cancer-Associated Fibroblasts^[9] (PCAF; 2,500 cells per well). The PCAF cells were a kind gift from Dr. Diane Simeone. Organoids were then incubated with 42.55 μ M lipid equivalent of Cet-PINs and untargeted constructs labeled with AF 680 in DMEM containing 10% FBS for 1, 6 or 24 h, followed by three 100 μ l washes in culture medium. The organoids were then fixed with 10% formalin for 10 min, followed by three 100 μ l washes in 1M glycine before confocal microscopy imaging.

To quantify the Cet-PIN specificity, the organoids were imaged using a 10x objective and a 635 nm laser with the highest acquisition parameter threshold set to the highest signal coming from organoids incubated with the Cet-PIN-Alexa680 at each time-point, across all the organoids. Z-stack images across a 75 μ m cross-section of the organoids were acquired, projected as sum of intensities of all images in the z-stack using ImageJ software and saved as tiff files for quantification. The tiffs (brightfield and fluorescence images) were processed in MATLAB (MathWorks Inc) using custom written segmentation-based algorithms^[10] to deduce PIN intensity as a function of organoid area. The sum of intensities/pixel for the Cet-PIN-treated organoids was divided by the intensity of the organoids incubated with the untargeted constructs to obtain normalized metrics for targeting specificity.

To visualize PIN penetration, the organoids were imaged using two-photon microscopy with a 40x objective and 800 nm excitation using a Mai Tai Laser. Acquisition was standardized to each individual organoid. Z-stack images across a 100 μ m cross-section of the organoids were acquired and projected in three-dimensional space using AMIRA (FEI Inc) 3D reconstruction software and customized color bars to display the organoids from different treatment groups. 2D cross-sections of the middle 50% Z-plane of each organoid was selected to evaluate the degree of organoid penetration.

NIR photodynamic activation in monotypic and heterotypic organoids, and CALYPSO image analysis for viability: MIA PaCa-2 monotypic organoids and MIA PaCa-2 – PCAF heterotypic organoids were prepared as described. 48h after seeding, the organoids were incubated with varying concentrations of BPD equivalent of Cet-PINs and untargeted constructs for 6 h, followed by three 100 μ l washes in culture medium. Organoids were then subject to 40 J/cm² of 690 nm laser light at an irradiance of 150 mW/cm². 72h following molecular targeted NIR photoactivation, the LIVE/DEAD Cell Viability reagent mixture was added to each organoid according to the manufacturer's protocol (Thermo Fisher Scientific) and the organoids were imaged using confocal microscopy. Images were analyzed using the previously reported Comprehensive high-throughput image analysis for quantifying the therapeutic efficacy in architecturally complex heterotypic organoids (CALYPSO).^[11] Untreated control organoids were used for thresholding of viability signals and total killing control organoids (formalin fixation, Triton X-100 permeabilization) were used for thresholding of dead cell signals. CALYPSO analysis generated viability heatmap images and empirical outputs of fractional viability. All treatment conditions were performed with an *n* of 4-8 organoids. For Cet-PINs encapsulating chemotherapy, heterotypic organoids were incubated with 1 μ M and 2 μ M BPD-PC equivalent of constructs for 6 h 24 h after seeding, prior to NIR photodynamic activation with 40 J/cm² of 690 nm laser light at an irradiance of 150 mW/cm². 72h following treatment, CALYPSO analysis was performed as described above.

In vivo Cet-PIN penetration and molecular targeted NIR photodynamic activation: Swiss nude mice were purchased from Cox7 at Massachusetts General Hospital. Subcutaneous heterotypic MIA Paca-2 + PCAF tumors were generating by implantation of a mixture of 1 x10⁶ cells of each cell line in 50 μ l of culture media and Matrigel (50% v/v). When the tumors reached ~50mm³, they were imaged using photoacoustic imaging (PAI) to generate baseline images of tumor vascularity.

The same mice were then intravenously injected with 5 nmol IRDye 800CW equivalent of Cet-PIN-IRDye800 constructs. 12 hours following administration, the tumors were imaged using PAI to generate 2D cross sections and 3D render images of the Cet-PIN penetration out of the vessels within the tumor.

For *in vivo* molecular targeted NIR photodynamic activation, mice were implanted with heterotypic MIA Paca-2 + PCAF tumors as described above. Cet-PIN constructs or untargeted constructs were administered *via* tail vein injection to the mice at a dose of 0.5 mg/kg BPD equivalent. 12 h following administration, the tumors were illuminated with NIR light for *in vivo* photodynamic activation of the constructs (690 nm, 150 J/cm², 100 mW/cm²). Tumors were harvested 72 h following molecular targeted and untargeted NIR photodynamic activation for histological analysis. The overlying skin, vicinal muscle, proximal liver and photodamaged bowel was also harvested for histological analysis. Tumors and tissue were cryosectioned and stained with hematoxylin and eosin (H&E) stains. Tumor cryosections were also stained with Masson's trichrome stain to visualize collagen. For visual clarity only, all images were evenly set to (0.8 Gamma, 136% brightness, 155% contrast, 72% red, 102% green, 102% blue.) Tumor necrosis and collagen in stained tumor slices were quantified from unaltered, as-acquired images using custom-developed MATLAB routines. Whole slide TIFF images obtained from the NanoZoomer imaging system were quantified using custom designed MATLAB routines as previously described in detail by our group^[12]. Specifically, the brightfield color images obtained from NanoZoomer imaging system were converted to gray scale and an Otsu threshold algorithm was used to identify tissue section boundaries to calculate the tumor cross section areas. The colored brightfield image was also analyzed via K space cluster analysis to isolate the tumor tissue stained areas (colored) from

necrotic zones (no color). A ratio of area of tumor tissue necrosis to total tumor cross-section area provided % necrosis per tumor cross-section.

SUPPLEMENTARY RESULTS

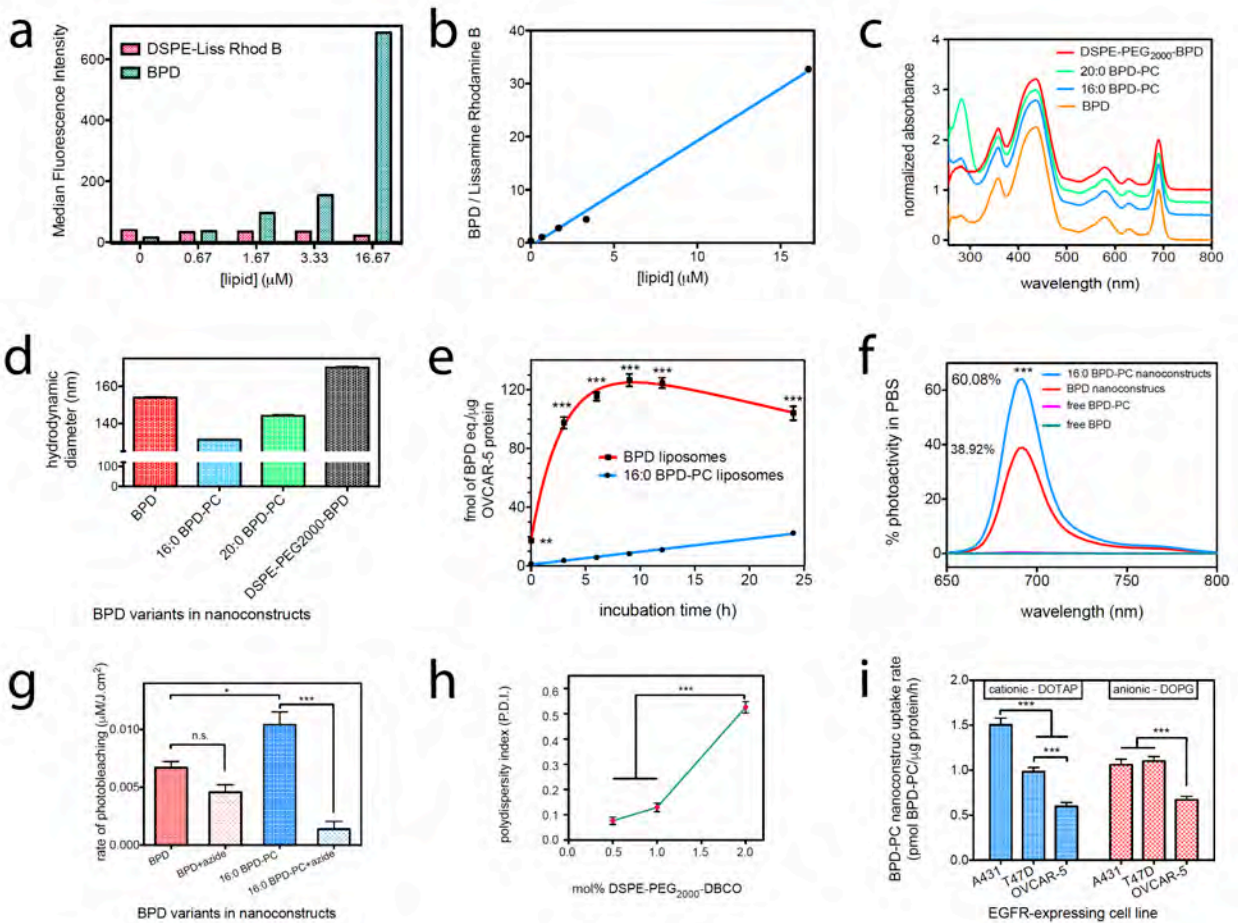


Figure S1. a) Median fluorescence intensities of BPD and DSPE-Lissamine Rhodamine B (DSPE-Liss Rhod B) in OVCAR-5 cells incubated for 30 min with increasing lipid concentration equivalents of nanoconstructs co-doped with BPD and the lipid anchored fluorophore DSPE-Liss Rhod B. b) A concentration-dependent increase in the BPD/Liss Rhod B ratio confirms that BPD leeches from the nanoconstruct liposomal bilayer into the cells. c) Normalized UV-Visible absorption spectra of free BPD and its lipidated variants DSPE-PEG₂₀₀₀-BPD, 20:0 BPD-PC and

16:0 BPD-PC diluted in DMSO confirm that no spectral shift of the photosensitizer occurs after conjugation to the lipids. The spectra are off-set by 0.25 for clarity. d) Hydrodynamic diameters of nanoconstructs formulated with BPD and its lipidated variants, demonstrating average diameters of 130-150 nm, whereas the DSPE-PEG₂₀₀₀-BPD doped nanoconstructs exhibit a larger diameter of ~170 nm. e) 16:0 lyso PC anchoring of BPD into nanoconstruct slows down the uptake of the sensitizer in OVCAR-5 cells over a 24 h incubation period. f) 16:0 BPD-PC nanoconstructs exhibit 21% greater fluorescence activity than BPD nanoconstructs and g) a 36% faster rate of photobleaching that is reduced in the presence of the singlet oxygen quencher sodium azide. h) polydispersity indices (P.D.I.s) measurements of BPD-PC nanoconstructs containing 5 mol% DSPE-mPEG₂₀₀₀ with incremental increases in DSPE-PEG₂₀₀₀-DBCO composition reveal an instability with 2 mol% DSPE-PEG₂₀₀₀-DBCO. i) Uptake rates of cationic (DOTAP) and anionic (DOPG) BPD-PC nanoconstructs in EGFR-expressing cell lines (A431 high, T47D low, OVCAR-5 high). (Mean \pm S.E.M., One-Way ANOVA with a Tukey Post-Test.)

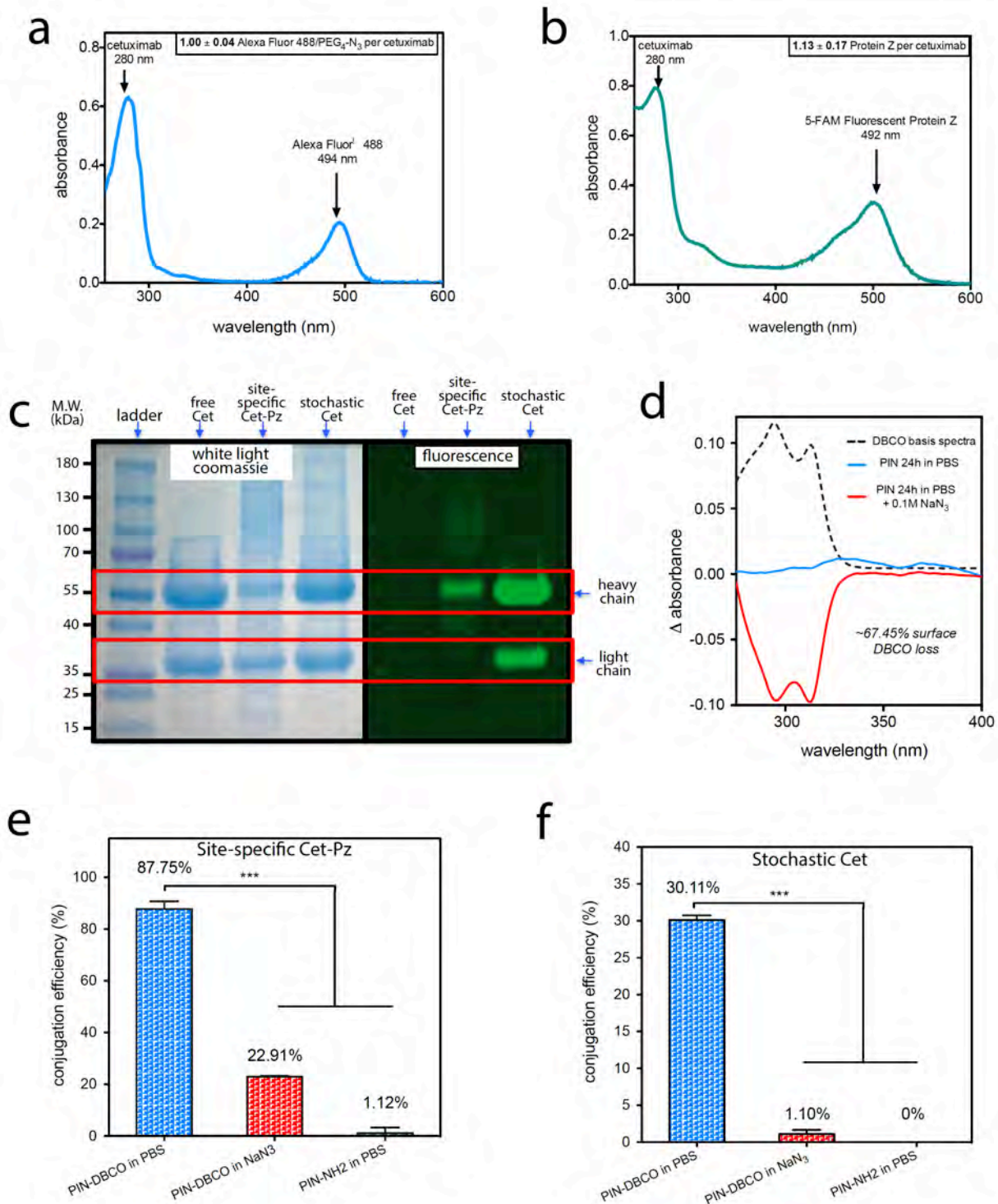


Figure S2. UV-visible absorption spectra of Cet stochastically modified with a single AF488 and single PEG₄-N₃ linker (a) or site-specifically modified with a single Pz molecule, fluorescently labeled with 5-FAM (b). c) Denaturing sodium dodecyl sulfate polyacrylamide gel electrophoresis

(SDS-PAGE) analysis of free Cet, Cet conjugated to Pz, and Cet conjugate to AF488 and PEG₄-N₃. Coomassie blue stain (GelCode Blue Safe Protein Stain, left) shows the heavy chains and light chains of Cet following the denaturing electrophoresis. Fluorescence imaging of the gels reveals 5-FAM fluorescence only from the heavy chain of the site-specific Pz conjugate, and AF488 fluorescence from both the heavy and light chains of the stochastic conjugate. Inactivation of 67.45% of the nanoconstruct surface DBCO using 0.1M NaN₃ (d) significantly reduces the conjugation efficiency of site-specific Cet-Pz (e) and stochastic Cet (f). Adsorption of either Cet-Pz or Cet to BPD-PC nanoconstructs void of DBCO is negligible. (Mean ± S.E.M., One-Way ANOVA with a Tukey Post-Test.)

Table S1. Physical characterization of PINs conjugated to site-specific Cet-Pz and stochastic Cet-PEG₄-N₃ at varying lipid : Cet mass ratios.

Conjugation Strategy	Lipid: Cet Mass Ratio	Z-average Diameter ^[a]	P.D.I. ^[b]	ζ-potential ^[c]	Cet per PIN	Cet density ^[d] surface
	1:0	138.1 (±7.2)	0.144 (±0.03)	-23.6 (±0.5)	0	0
Cet-Pz	1:0.02	151.4 (±7.6)	0.134 (±0.03)	-22.6 (±0.4)	13.8 (±2.2)	191.6 (±30.6)
	1:0.05	161.9 (±24.0)	0.147 (±0.03)	-22.7 (±0.5)	31.3 (±3.2)	380.1 (±38.9)
	1:0.10	161.0 (±23.0)	0.156 (±0.07)	-21.7 (±0.6)	61.9 (±5.1)	760.1 (±62.6)
	1:0.15	164.6 (±22.5)	0.171 (±0.03)	-21.0 (±1.0)	84.7 (±7.4)	995.1 (±86.9)
	1:0.20	167.9 (±13.1)	0.165 (±0.01)	-19.8 (±1.0)	100.0 (±5.9)	1129.14 (±66.6)
	Cet-PEG ₄ -N ₃	1:0.02	138.0 (±16.2)	0.135 (±0.05)	-22.9 (±0.8)	4.2 (±1.0)
1:0.05		145.7 (±24.0)	0.139 (±0.04)	-22.5 (±0.6)	8.6 (±3.5)	129.0 (±52.5)
1:0.10		157.0 (±30.8)	0.214 (±0.10)	-21.9 (±0.9)	18.0 (±6.4)	232.5 (±82.6)
1:0.15		134.8 (±4.0)	0.097 (±0.00)	-20.1 (±1.8)	23.1 (±4.3)	404.7 (±75.3)
1:0.20		134.7 (±11.0)	0.092 (±0.06)	-20.5 (±0.7)	29.5 (±7.9)	517.5 (±138.6)

[a] nanometers (nm), [b] polydispersity index, [c] millivolts (mV), [d] Cet per μm^2 . Values are mean (± S.D.)

Table S2. Efficacy of molecular targeted NIR photodestruction in cells with varying degrees of EGFR expression using Cet-PINs and untargeted constructs, irradiated with 690 nm light (20 J/cm² at 150 mW/cm²).

Cell Line	IC ₅₀ with untargeted construct ^[a]	IC ₅₀ with Cet-PINs ^[a]	Fold Reduction in IC ₅₀	% IC ₅₀ of untargeted construct
MIA PaCa-2	271.4	9.3	29.2	3.4
OVCAR-5	548.7	70.9	7.7	12.9
A431	489.9	105.0	4.7	21.4
T47D	798.5	563.2	1.4	60.7
CHO-WT	3229.5	4649.8	0.7	144.0
CHO-EGFR	3717.7	5.4	688.5	0.1

[a] nanomolar (nM) BPD-PC equivalent. (mean values).

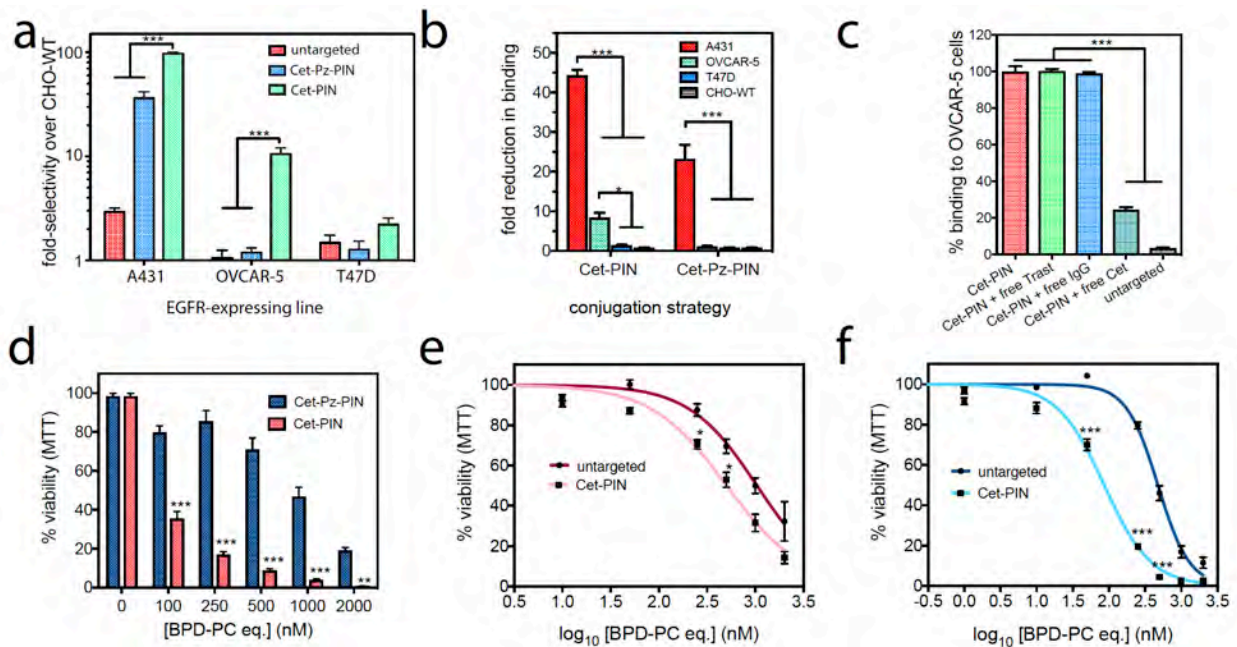


Figure S3. a) The binding selectivity of unconjugated construct, Cet-Pz-PIN and Cet-PIN to A431, OVCAR-5 and T47D cells are presented with respect to EGFR-null CHO-WT cells. b) Degree of reduction in binding of Cet-PIN and Cet-Pz-PIN constructs to A431, OVCAR-5, T47D and CHO-WT cells by the presence of 1 mg/ml free Cet that matches the concentration of free human IgG in the serum-containing media. c) Competitive inhibition of Cet-PIN binding to OVCAR-5 cells using 100x free Cet reduces PIN binding by 80%, yet binding is unaltered in the presence of 100x free Trastuzumab or free IgG sham. d) Difference in molecular targeted NIR photodestruction of OVCAR-5 cells treated with the Cet-PIN construct and the Cet-Pz PIN construct. Phototoxicity dose response curves of T47D (e) and A431 (f) cells treated with an untargeted construct and the optimal Cet-PIN construct. All values are mean \pm S.E.M., One-Way ANOVA with a Tukey Post-Test.

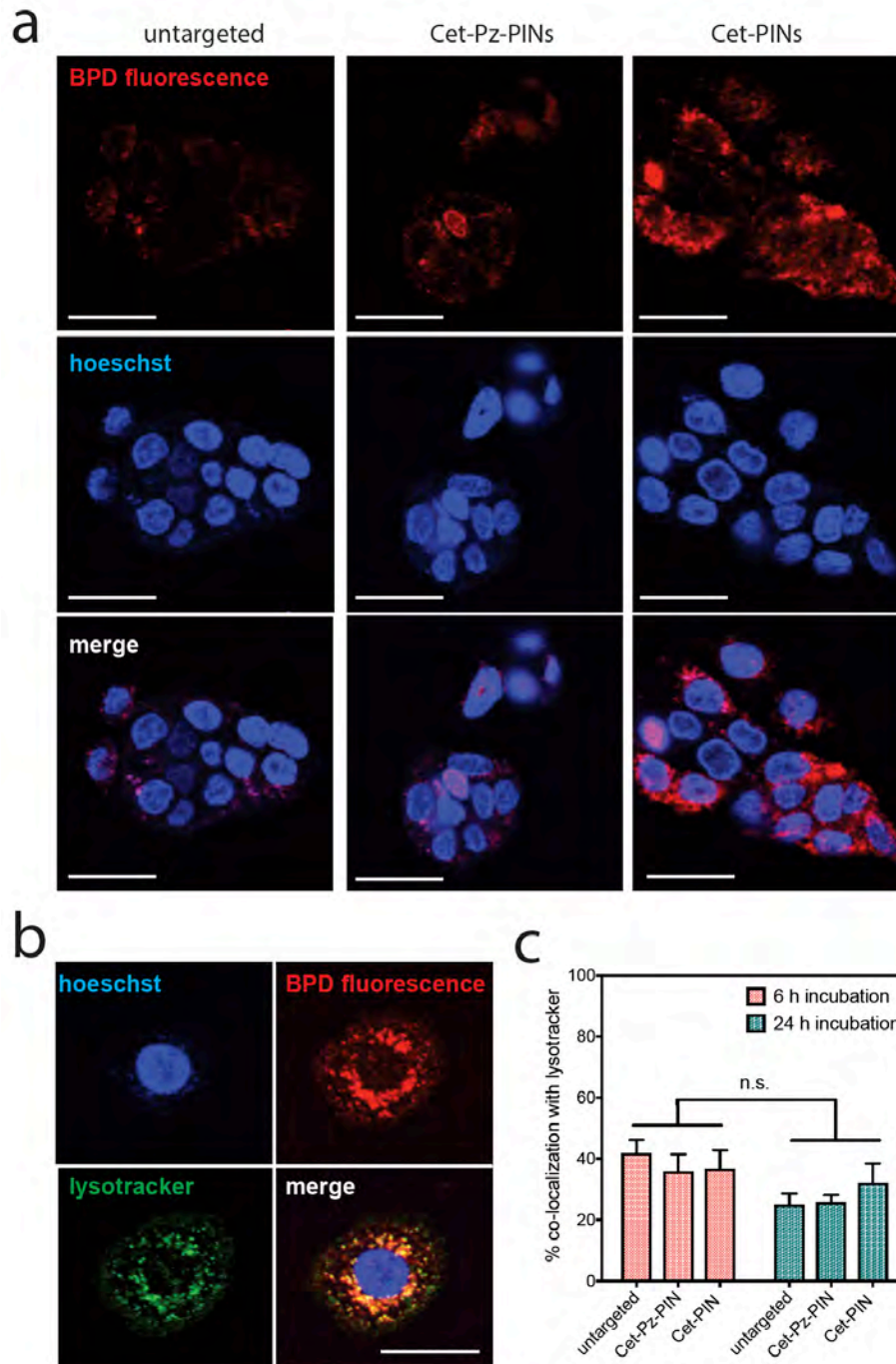


Figure S4. a) Confocal images (60x) of OVCAR-5 cells incubated for 6 h with untargeted (left), Cet-Pz-PIN (center) and Cet-PIN (right) constructs. b) Visual lysosomal colocalization of Cet-PIN constructs in OVCAR-5 cells. (Scale bars are 50 μm) c) Quantification of lysosomal co-

localization of untargeted, Cet-Pz-PIN and Cet-PIN constructs at 6 h and 24 h incubation times.
(mean \pm S.E.M., n=8, One-Way ANOVA with a Tukey Post-Test.)

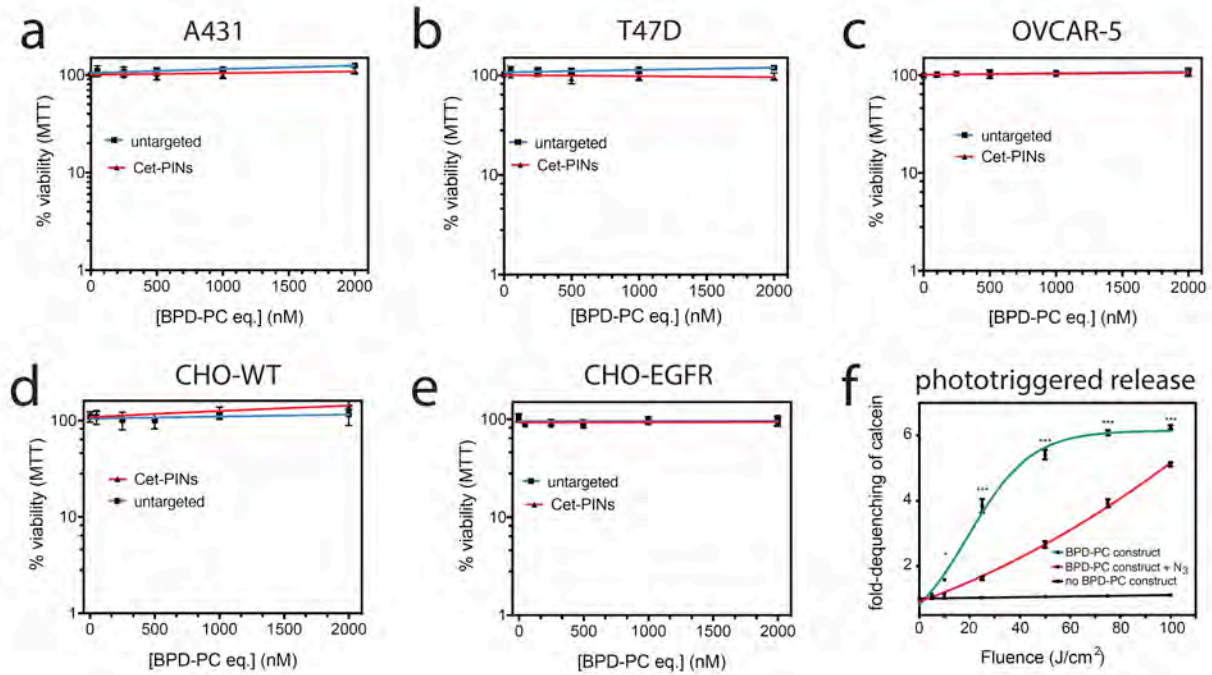


Figure S5. Absence of dark toxicity of untargeted constructs and the Cet-PINs in A431 (a), T47D (b), OVCAR-5 (c), CHO-WT (d) and CHO-EGFR cells (e) treated for a 6 h pulse, followed by 72 h incubation. Viability was measured using the MTT assay. f) Phototriggered release of entrapped quenched calcein disodium salt is inhibited by the presence of 10 mM sodium azide, confirming that release is largely dependent on photochemical activation of BPD-PC. (values are mean \pm S.E.M.; One-Way ANOVA with a Tukey Post-Test.)

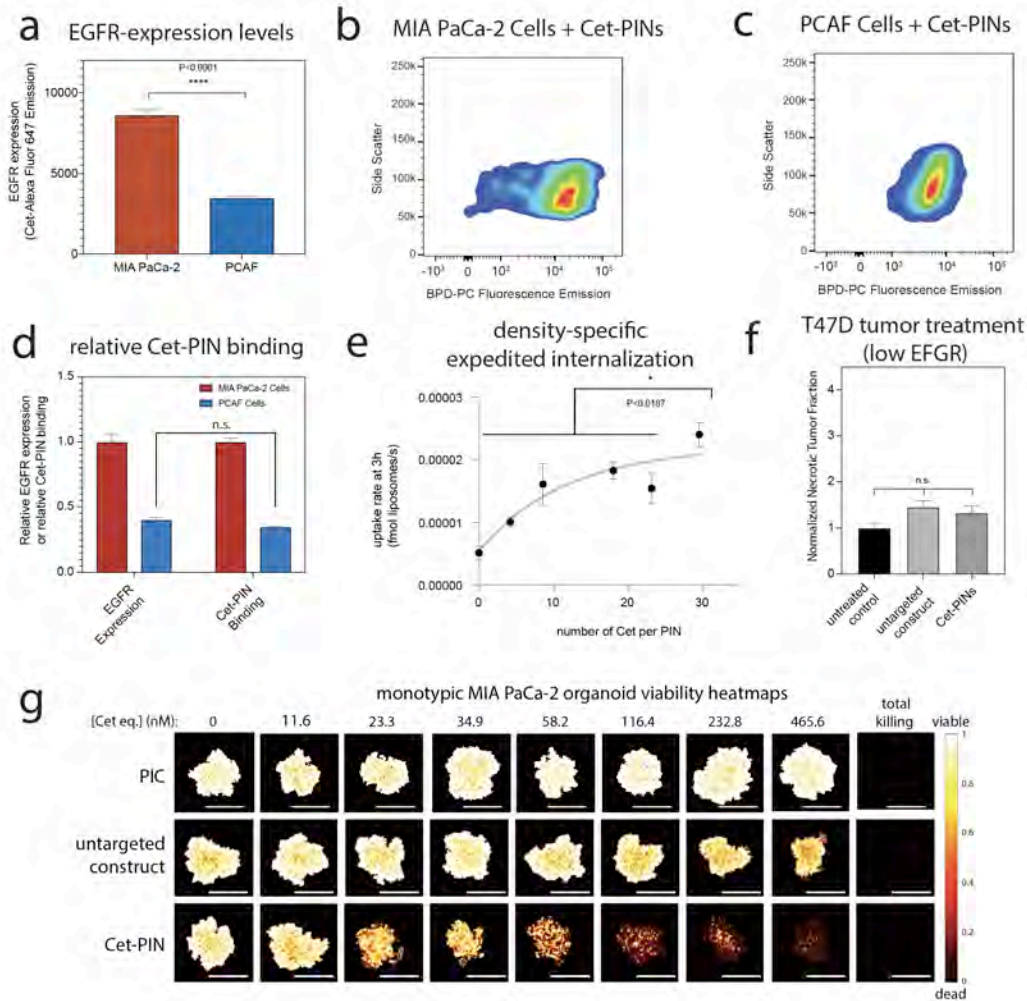


Figure S6. a) EGFR expression in MIA PaCa-2 cells and PCAF cells determined using flow cytometry, depicted as the median fluorescence emission of AF680 conjugated to Cet. Representative flow cytometry plots of MIA PaCa-2 cells (b) and PCAF (c) cells incubated with Cet-PINs. d) A comparison between relative EGFR expression levels in MIA PaCa-2 cells and PCAF cells with the relative binding of Cet-PINs to the two cell lines. e) Cet-PINs exhibit ligand-density specific expedition of cellular internalization rates in OVCAR-5 cells. f) Photodynamic activation of Cet-PINs and untargeted constructs does not induce tumor necrosis in low EGFR-expressing T47D tumors. g) Viability heatmap images of monotypic PDAC organoids following molecular targeted NIR photodynamic activation with increasing concentrations of PIC,

untargeted construct and the specificity-tuned Cet-PIN (mean \pm S.E.M. and n=3 for a-d and f, n=4 for e and g, One-Way ANOVA with a Tukey Post-Test.)

Phototoxicology of untargeted constructs

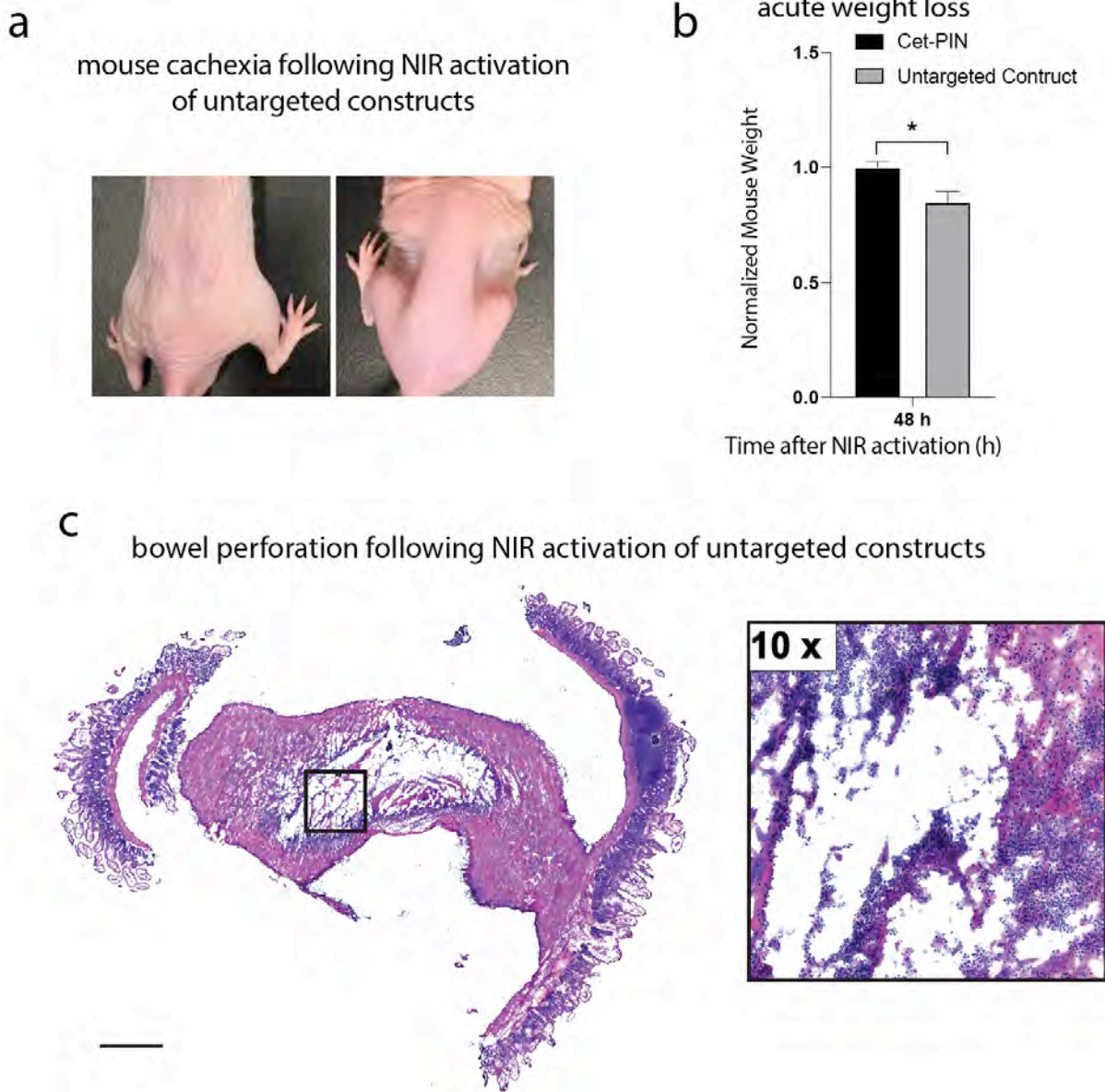


Figure S7. a) Representative photograph of mouse cachexia 72h following NIR photodynamic activation of untargeted constructs administered to mice bearing MIA PaCa-2 + PCAF heterotypic tumors (right), as compared to untreated mice (left). b) Acute weight loss of mice 72h following

NIR photodynamic activation of untargeted constructs, whereas untreated mice and mice treated with NIR photodynamic activation of Cet-PINs exhibited no change in body mass (two-tailed *t* test, * = $P < 0.05$). c) Bowel perforation evident from H&E stained tissue sections of visibly ulcerating bowel tissue 72h following NIR photodynamic activation of untargeted constructs administered to mice bearing MIA PaCa-2 + PCAF heterotypic tumors. (Scale bars is 1 mm.)

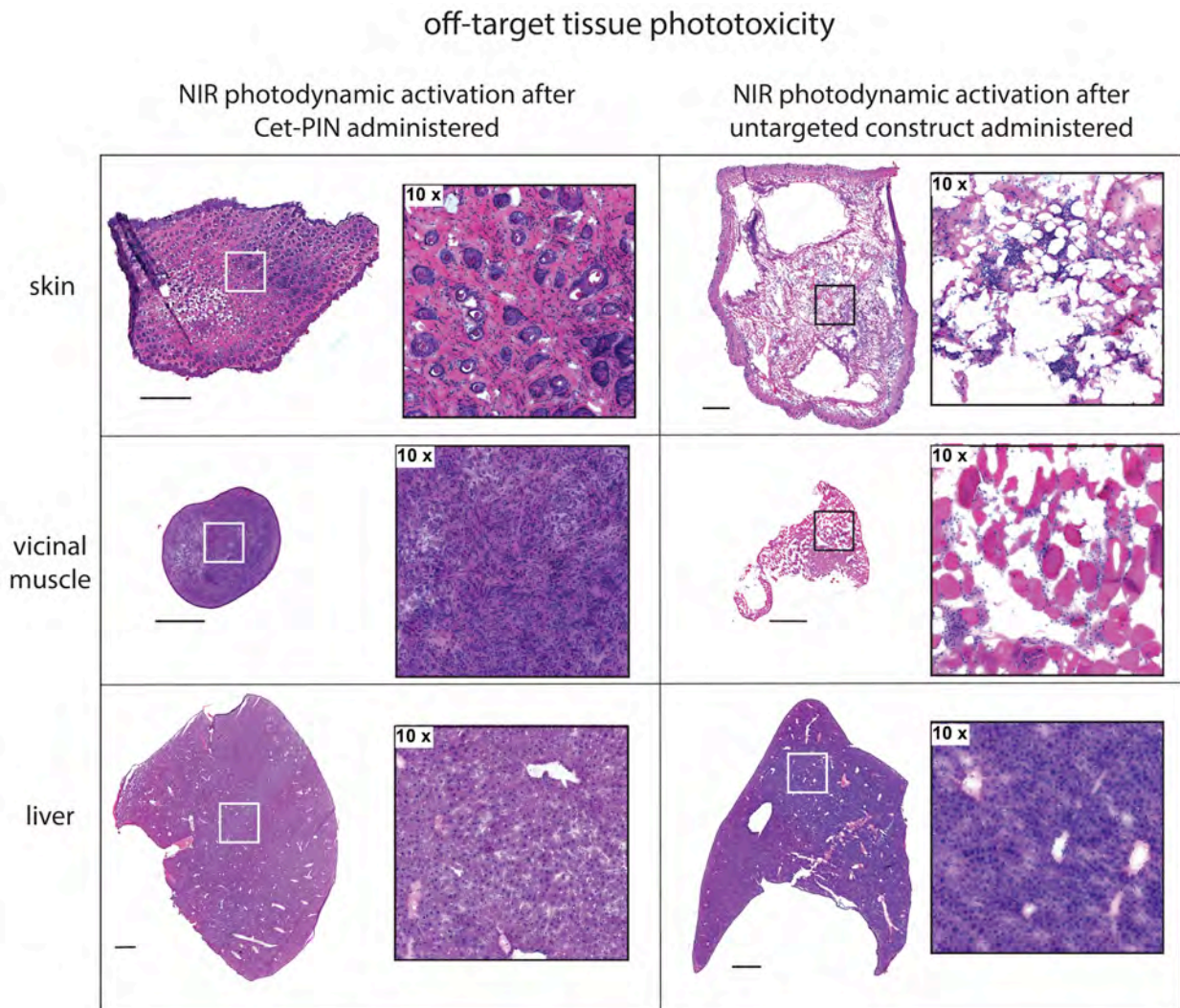


Figure S8. H&E stained tissue sections of skin directly covering MIA PaCa-2 + PCAF heterotypic tumors, vicinal muscle, and proximal liver tissue following NIR photodynamic activation of the specificity-tuned Cet-PINs or untargeted constructs. NIR photodynamic activation of untargeted

constructs induced significant tissue necrosis in skin covering the tumor and vicinal muscle, whereas NIR photodynamic activation of the Cet-PINs induced no off-target phototoxicity. The parts of the liver in close proximity to the site of NIR photodynamic activation was unaffected. Scale bars are 1mm.

REFERENCES

- [1] R. Warden-Rothman, I. Caturegli, V. Popik, A. Tsourkas, *Anal. Chem.* **2013**, *85*, 11090-11097.
- [2] J. Z. Hui, A. Tsourkas, *Bioconjug. Chem.* **2014**, *25*, 1709-1719.
- [3] M. R. Wilkins, E. Gasteiger, A. Bairoch, J. C. Sanchez, K. L. Williams, R. D. Appel, D. F. Hochstrasser, *Methods Mol. Biol.* **1999**, *112*, 531-552.
- [4] J. F. Lovell, C. S. Jin, E. Huynh, T. D. MacDonald, W. Cao, G. Zheng, *Angew. Chem., Int. Ed.* **2012**, *51*, 2429-2433.
- [5] G. Obaid, W. Jin, S. Bano, D. Kessel, T. Hasan, *Photochem. Photobiol.* **2018**.
- [6] aM. A. Jones, P. K. Kilpatrick, R. G. Carbonell, *Biotechnol. Prog.* **1993**, *9*, 242-258; bF. J. Hutchinson, S. E. Francis, I. G. Lyle, M. N. Jones, *Biochim. Biophys. Acta* **1989**, *978*, 17-24.
- [7] T. Heitner, A. Moor, J. L. Garrison, C. Marks, T. Hasan, J. D. Marks, *J. Immunol. Methods* **2001**, *248*, 17-30.
- [8] K. M. Morrill, H. D. Tyler, *Animal Industry Report* **2012**, *658*, 40.
- [9] M. Waghray, M. Yalamanchili, M. Dziubinski, M. Zeinali, M. Erkkinen, H. Yang, K. A. Schradle, S. Urs, M. Pasca Di Magliano, T. H. Welling, P. L. Palmbo, E. V. Abel, V. Sahai, S. Nagrath, L. Wang, D. M. Simeone, *Cancer Discov.* **2016**, *6*, 886-899.
- [10] aS. Mallidi, Z. Mai, I. Rizvi, J. Hempstead, S. Arnason, J. Celli, T. Hasan, *J. Biomed. Opt.* **2015**, *20*, 048003; bC. A. Schneider, W. S. Rasband, K. W. Eliceiri, *Nat. Methods* **2012**, *9*, 671-675.
- [11] A. L. Bulin, M. Broekgaarden, T. Hasan, *Sci. Rep.* **2017**, *7*, 16645.
- [12] S. Mallidi, Z. Mai, I. Rizvi, J. Hempstead, S. Arnason, J. P. Celli, T. Hasan, *J. Biomed. Opt.* **2015**, *20*, 048003.